Properties of Dark Matter Halos

- Halo Mass and Velocity functions
- Halo Profiles
- Halo Concentrations
- Abundance of subhalos
- Density and velocity around halos

Halo Mass and Velocity functions

rms density fluctuation: $$\sigma^2(M) = \frac{b^2(z)}{2\pi^2}\int_0^\infty k^2 P(k) W^2(k;M)\,\mathrm{d}k,$$

P(k) = Power spectrum of fluctuations, k = wavenumber

$W^2(k;M)$ = Fourier spectrum of top-hat filter with mass M and radius R

b(z) = growth rate of fluctuations according to the linear theory normalized to b(z=0) = 1.

Functional form for mass function:

$$\frac{dn}{dM} = f(\sigma)\,\frac{\bar{\rho}_m}{M}\,\frac{d\ln\sigma^{-1}}{dM}$$

Average matter density:

$$\bar{\rho}_m(z) \equiv \Omega_m(z)\rho_{\rm crit}(z) = \bar{\rho}_m(0)(1+z)^3$$

Numerical factor:

$$f_{\rm P-S}(\sigma) = \sqrt{\frac{2}{\pi}}\,\frac{\delta_{\rm c}}{\sigma}\exp\left(-\frac{\delta_{\rm c}^2}{2\sigma^2}\right)$$

$$\delta_{\rm c} = 1.686$$

$$f_{\rm S-T}(\sigma) = A\sqrt{\frac{2a}{\pi}}\left[1+\left(\frac{\sigma^2}{a\delta_{\rm c}^2}\right)^p\right]\frac{\delta_{\rm c}}{\sigma}\exp\left(-\frac{a\delta_{\rm c}^2}{2\sigma^2}\right)$$

$$A = 0.3222,\ a = 0.707 \text{ and } p = 0.3$$

rms density fluctuation:

$$\sigma^2(M) = \frac{b^2(z)}{2\pi^2}\int_0^\infty k^2 P(k) W^2(k; M)\,{\rm d}k,$$

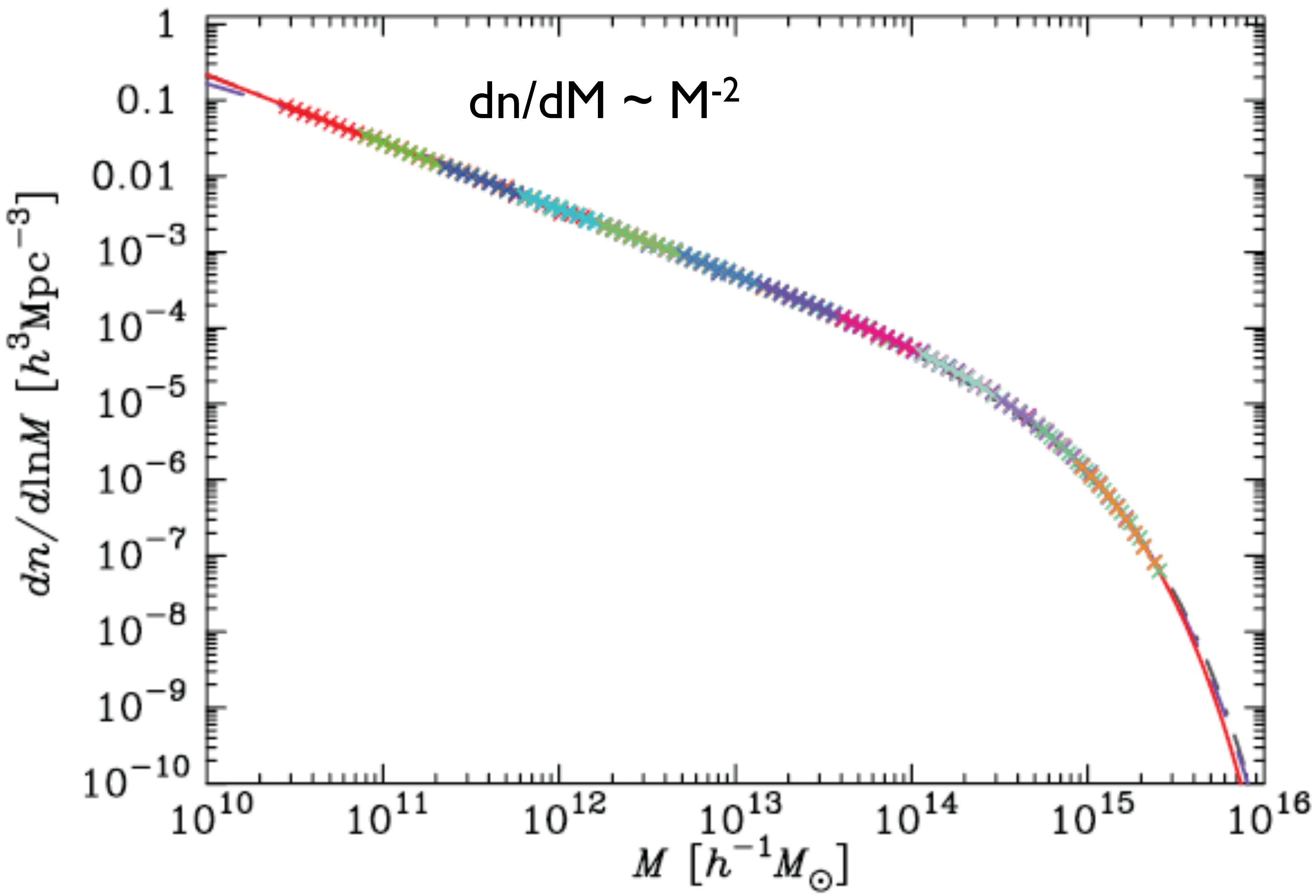

Warren et al 2006

FIG. 1.—Central values of the binned mass functions from sixteen 1024^3 simulations of the ΛCDM universe as crosses, with simulations in different colors. The best-fit form for the mass function we calculate is shown as a solid line (*red*), the Jenkins fit as a dashed line (*purple*), and the Sheth-Tormen fit as a dot-dashed line (*dark gray*). Goodness of fit is poorly judged on this extreme log scale; it is more clearly resolved in the linear residuals of Fig. 2.

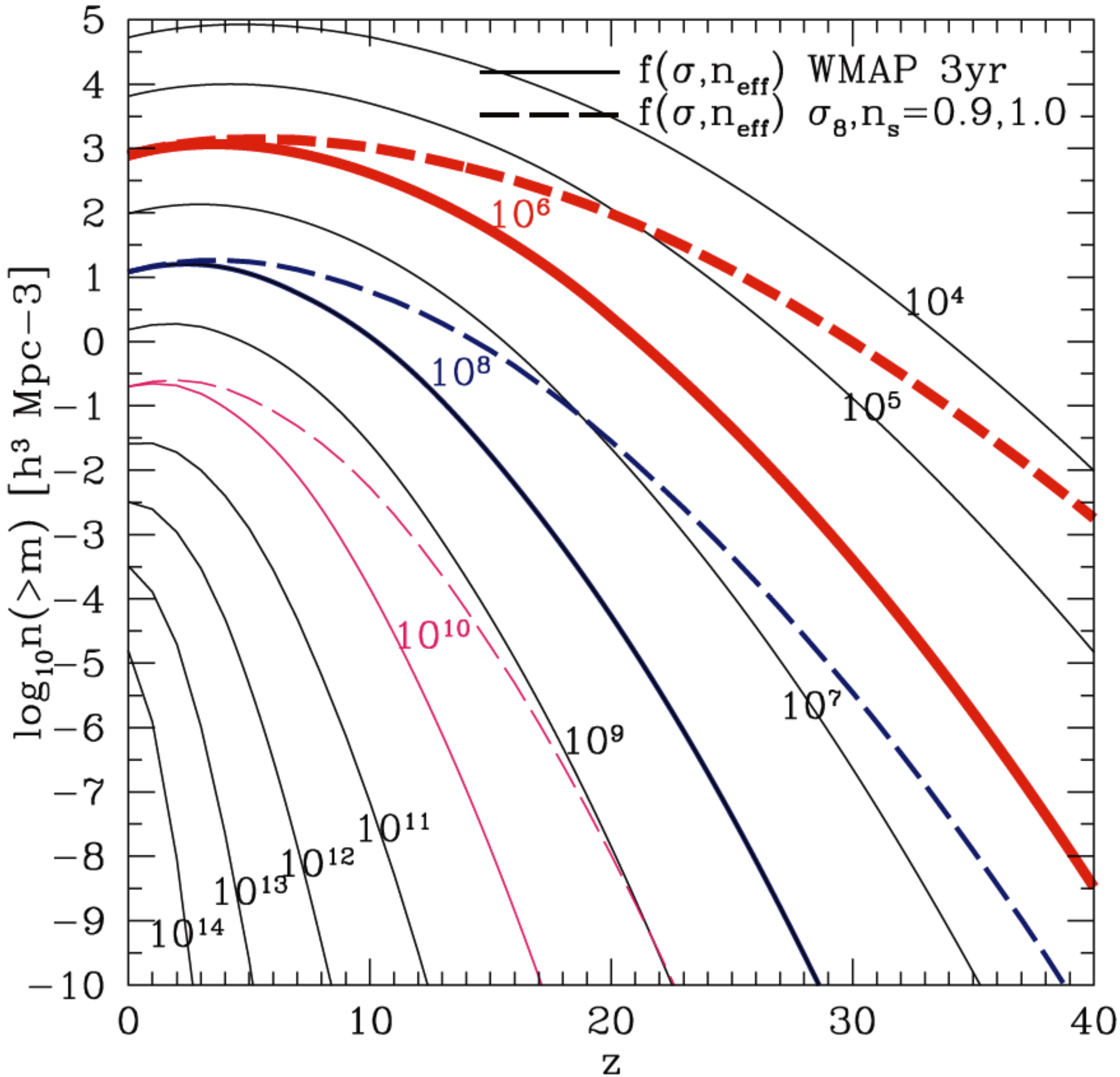

f(σ,n_eff) WMAP 3yr
f(σ,n_eff) σ_8,n_s=0.9,1.0
log_10 n(>m) [h^3 Mpc−3]
z
10^4
10^5
10^6
10^7
10^8
10^9
10^10
10^11
10^12
10^13
10^14

Halo mass function at z=0

Note the vertical axis scaling: the main trend of the mass function - $dn/dM \sim M^{-2}$ - has been taken away. We are looking at the deviations from the power-law.

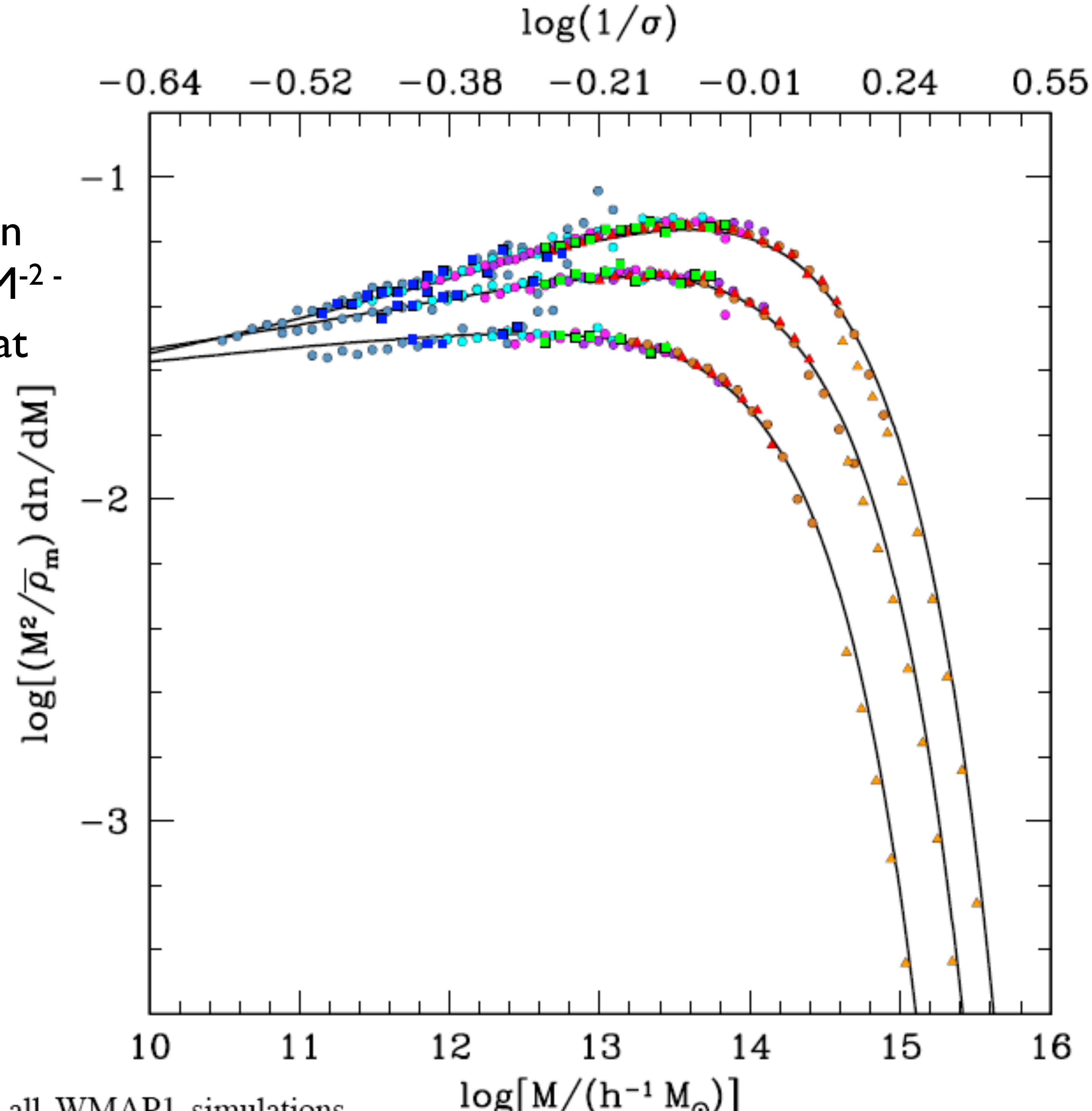

FIG. 5.— The measured mass functions for all WMAP1 simulations, plotted as $(M^2/\bar{\rho}_m)\,dn/dM$ against $\log M$. The solid curves are the best-fit functions from Table 2. The three sets of points show results for $\Delta = 200$, 800, and 3200 (from top to bottom). To provide a rough scaling between M and σ^{-1}, the top axis of the plot shows σ^{-1} for this mass range for the WMAP1 cosmology. The slight offset between the L1280 results and the solid curves is due to the slightly lower value of $\Omega_m = 0.27$.

Tinker etal 2008

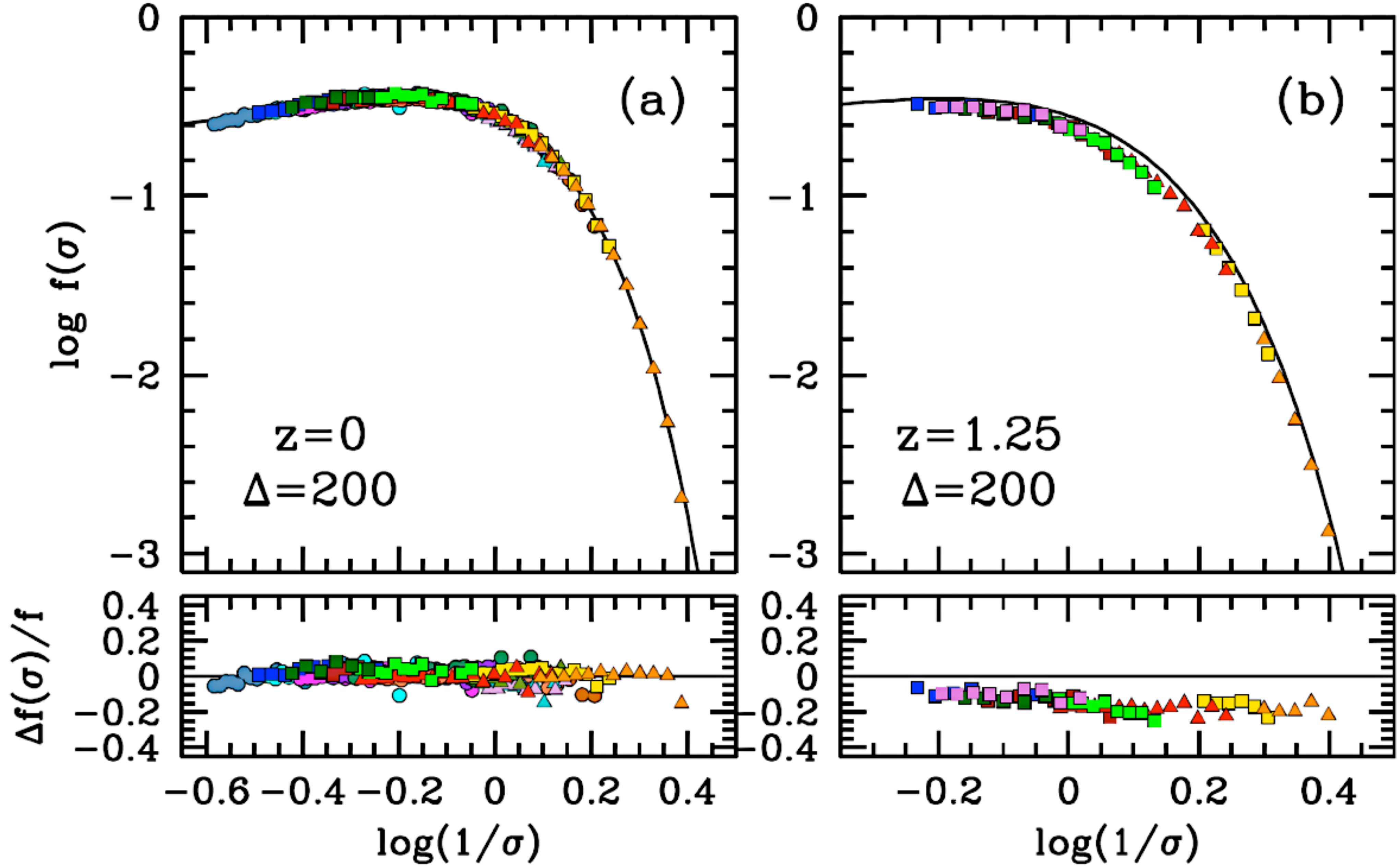

Nearly universal shape of mass function when we plot $f(\sigma)$

$$\frac{dn}{dM} = f(\sigma)\,\frac{\bar{\rho}_m}{M}\,\frac{d\ln\sigma^{-1}}{dM}$$

Evolution of the mass function with redshift

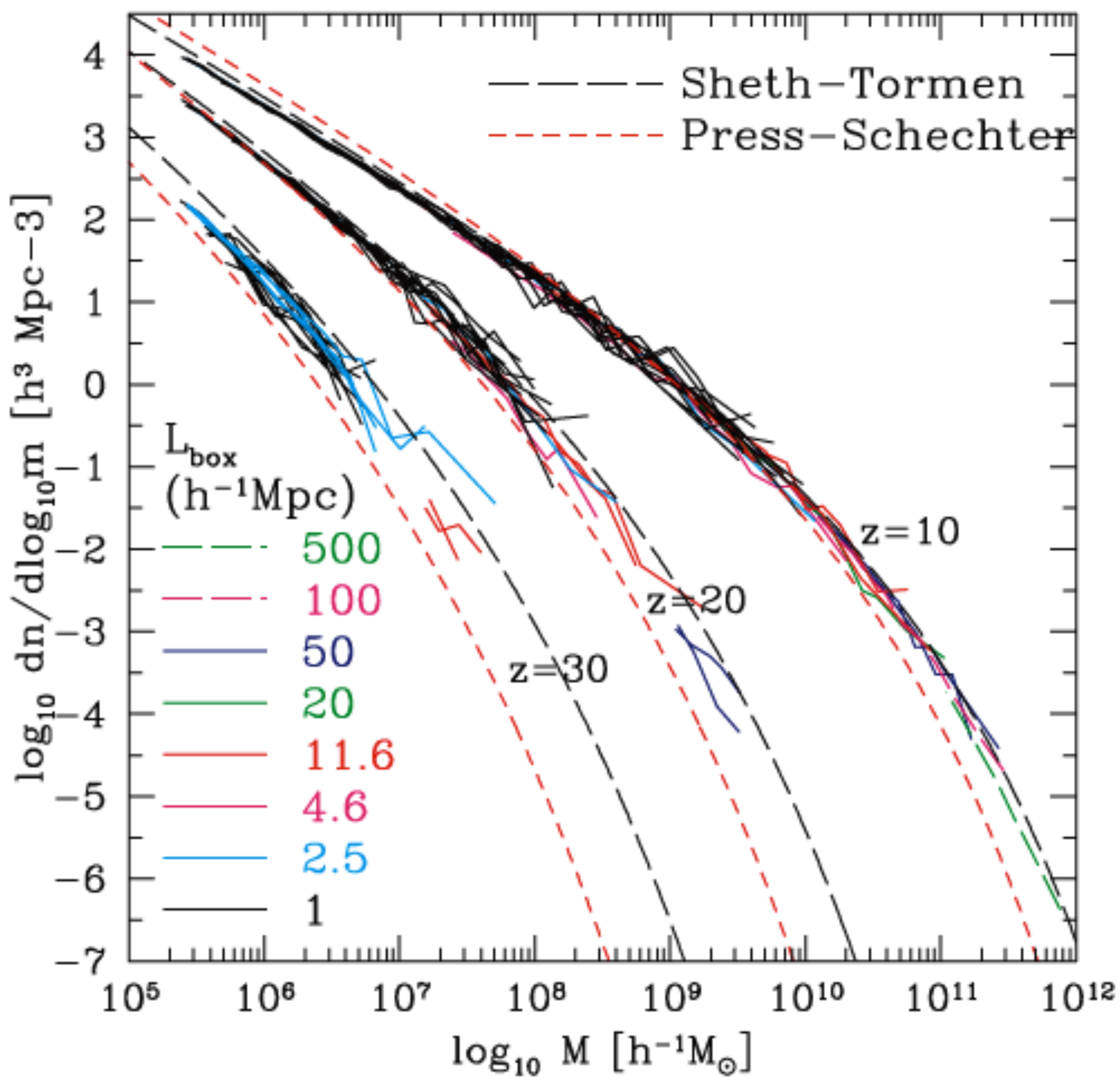

Read et al 2007

Evolution of the mass function with redshift

Full curves are for the Sheth-Torman approximation

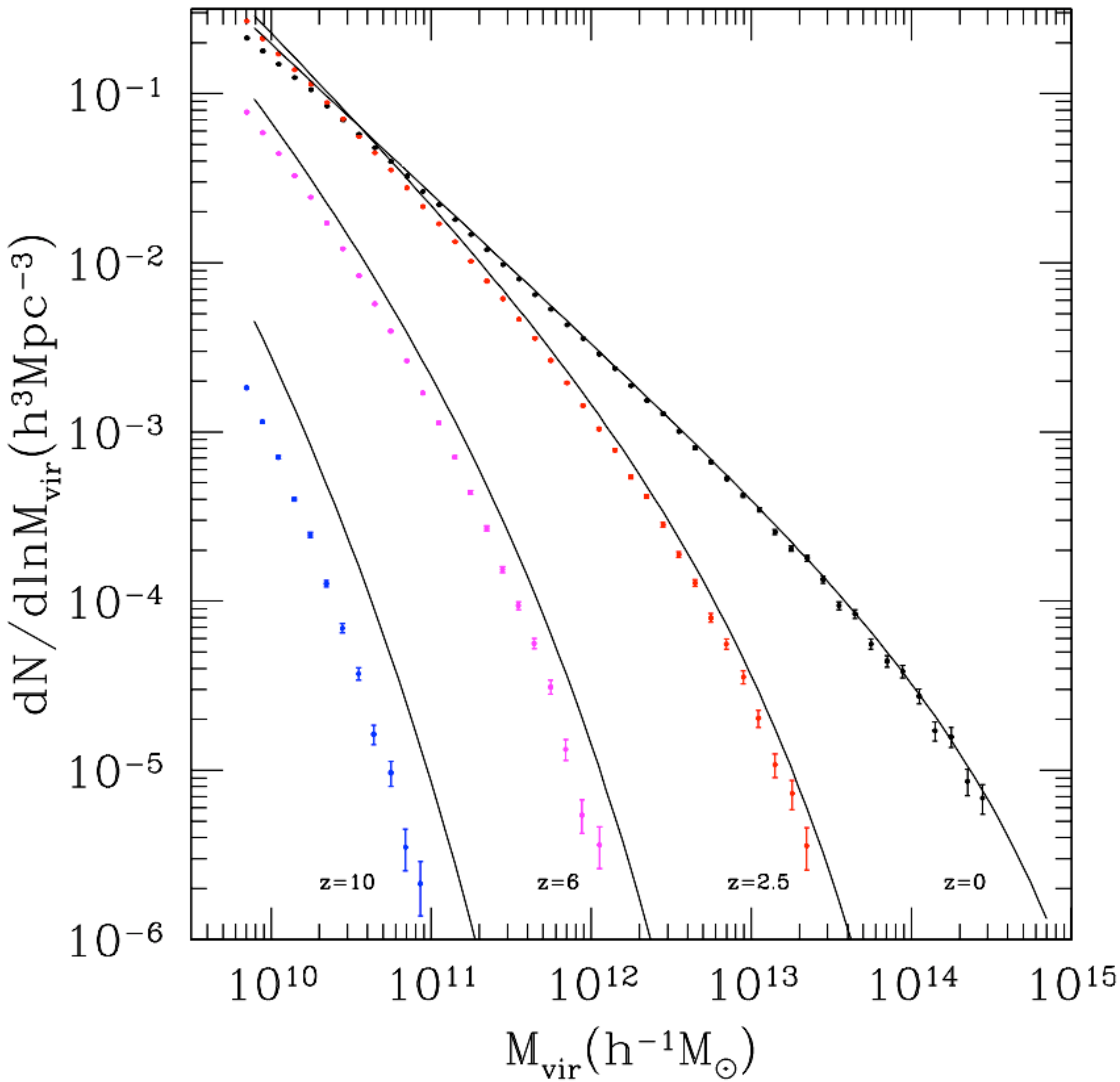

Symbols are from N-body simulations for distinct halos defined using Spherical Overdensity algorithm

Halo Velocity function

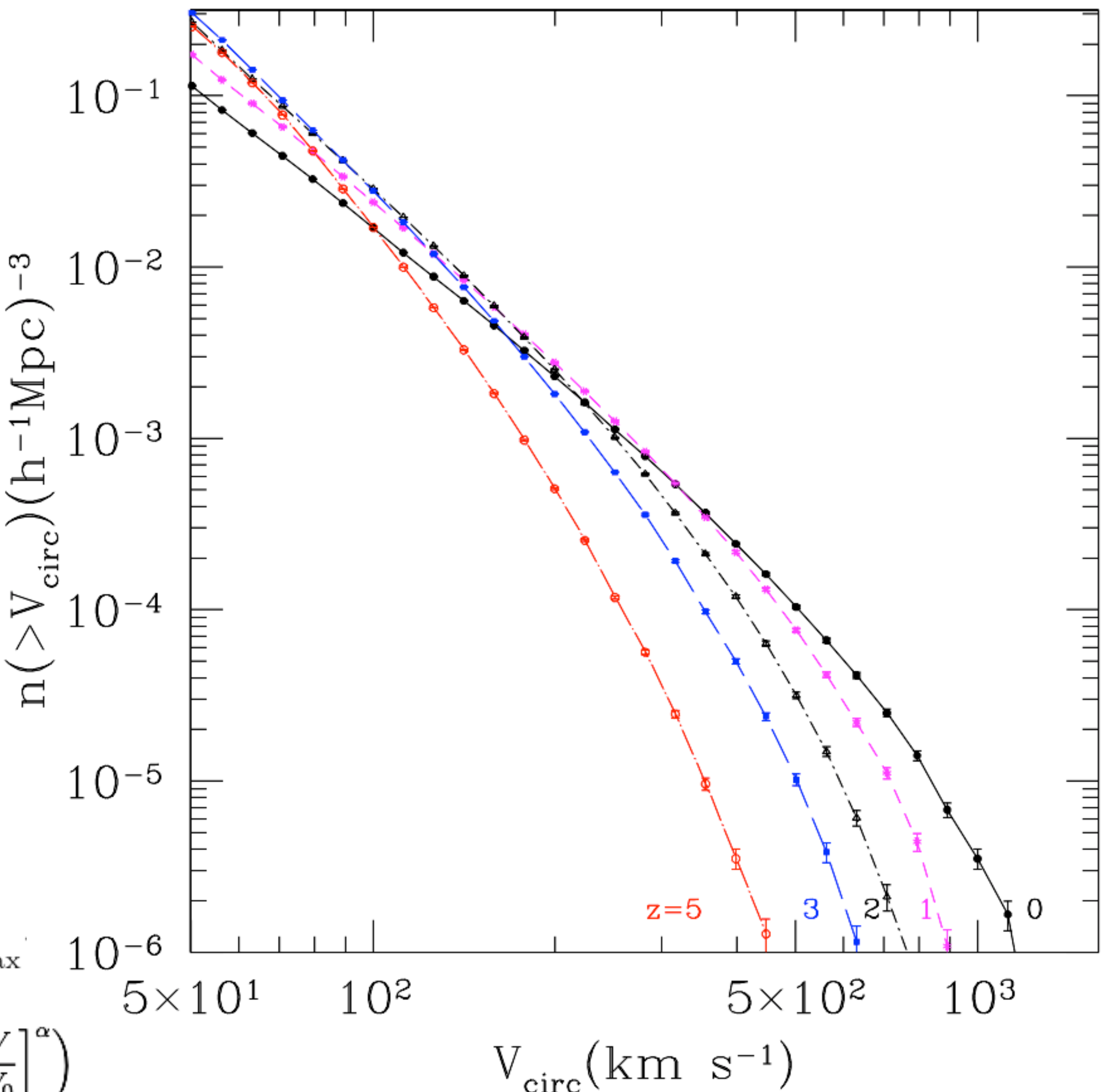

$$V_{\rm circ} = \sqrt{\frac{GM(<r)}{r}}\bigg|_{\rm max}$$

$$n(>V) = AV^{-3}\exp\left(-\left[\frac{V}{V_0}\right]^{\alpha}\right)$$

Halo Profiles

NFW

$$\rho(r) = \frac{\rho_0 r_s^3}{r(r + r_s)^2}\,, \quad M(r) = M_{\rm vir} \times \frac{f(x)}{f(C)}\,,$$

$$f(x) \equiv \ln(1 + x) - \frac{x}{1 + x}\,, \quad x \equiv \frac{r}{r_s}\,,$$

$$C \equiv \frac{r_{\rm vir}}{r_s}\,,$$

$$r_{\rm vir}(M_{\rm vir}) = 443\ h^{-1}\ {\rm kpc}\left(\frac{M_{\rm vir}/10^{11}\ h^{-1}\ M_\odot}{\Omega_0\,\delta_{\rm th}}\right)^{1/3}$$

$$M_{\rm vir} \equiv \frac{4\pi}{3}\,\rho_{\rm cr}\,\Omega_0\,\delta_{\rm th}\,r_{\rm vir}^3\,.$$

$$V_{\rm max}^2 = \frac{GM_{\rm vir}}{r_s} \times \frac{f(2)}{2f(C)}\,, \quad f(2) \approx 0.432\,,$$

$$M(r) = \frac{r_s\,V_{\rm max}^2}{G} \times \frac{2f(x)}{f(2)}\,, \quad \Omega^2(r) = \frac{V_{\rm max}^2}{r_s^2} \times \frac{2f(x)}{x^3 f(2)}\,,$$

$$V_{\rm esc}^2 = -2\phi(r) = 4V_{\rm max}^2 \times \frac{\ln(1 + x)}{xf(2)}\,,$$

$$\Omega^2(r) = \frac{GM}{r^3} = \frac{GM_{\rm vir}}{r_s^3 f(C)} \times \frac{f(x)}{x^3}\,,$$

$$\phi(r) = -\frac{GM_{\rm vir}}{r_s\,f(C)} \times \frac{f(x) + x/(1 + x)}{x}$$

$$\ln(\rho_\alpha/\rho_{-2}) = (-2/\alpha)[(r/r_{-2})^\alpha - 1].$$ Einasto

$$\rho_{-2} = \rho_s/4$$

$$r_{-2} = r_s.$$

$$\alpha = 0.2$$

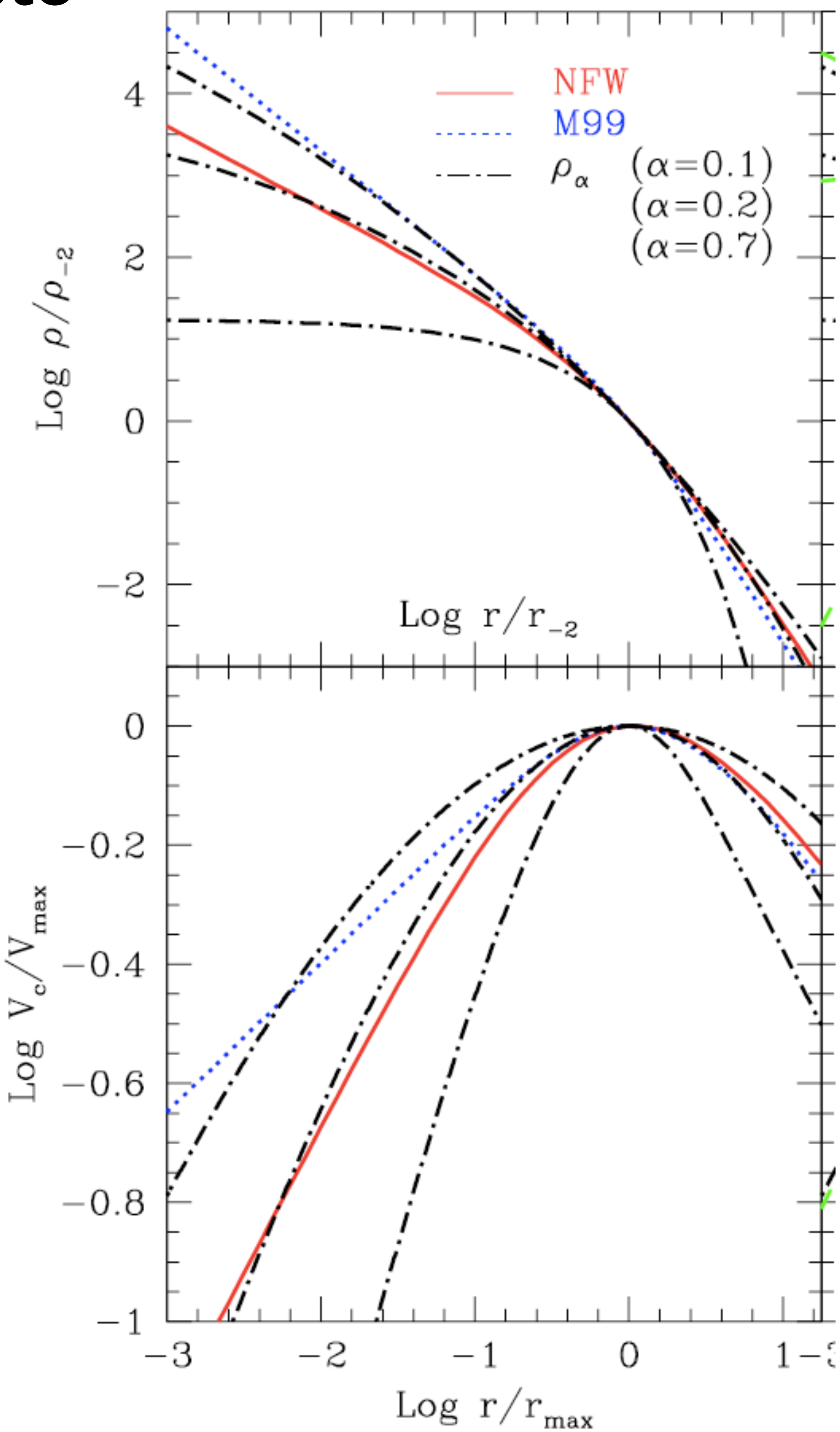

Navarro etal 2004

Dark matter profiles

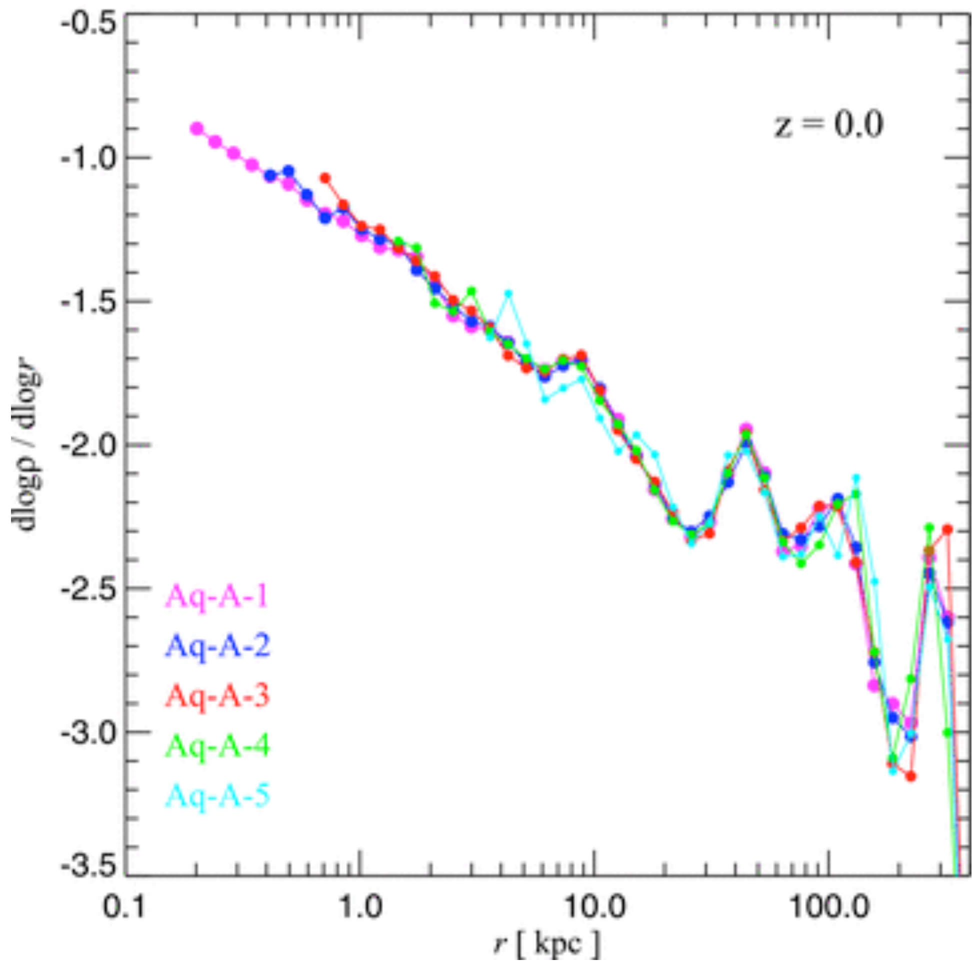

Aquarius simulation. Springel et al 2008. WMAP-1

Central slope is very close to -1

For normal galaxies it does not matter: baryons dominate

100pc

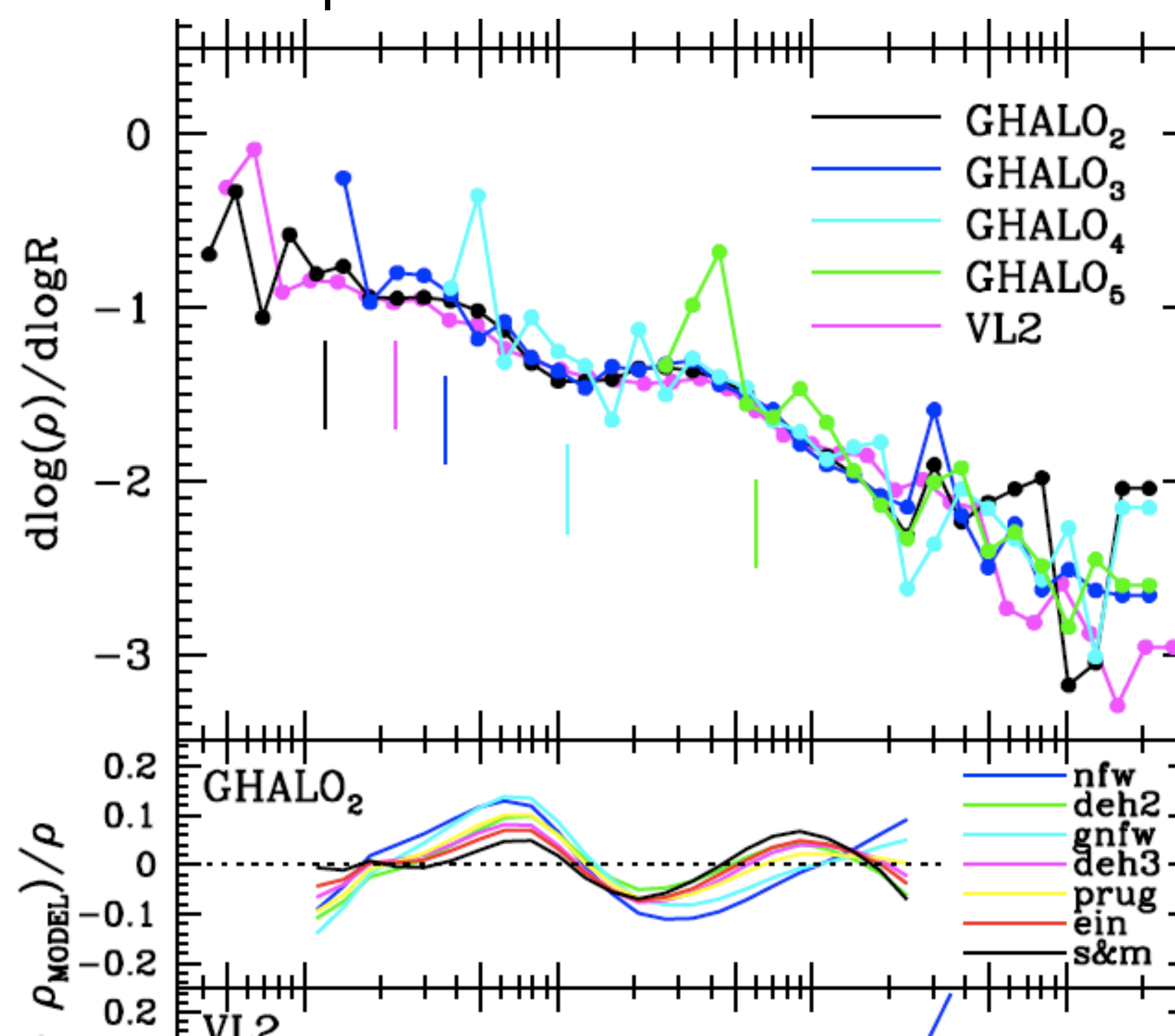

Stadel etal 2009

Properties of Dark Matter Halos :2

- Halo Concentrations
- Abundance of subhalos
- Density and velocity around halos

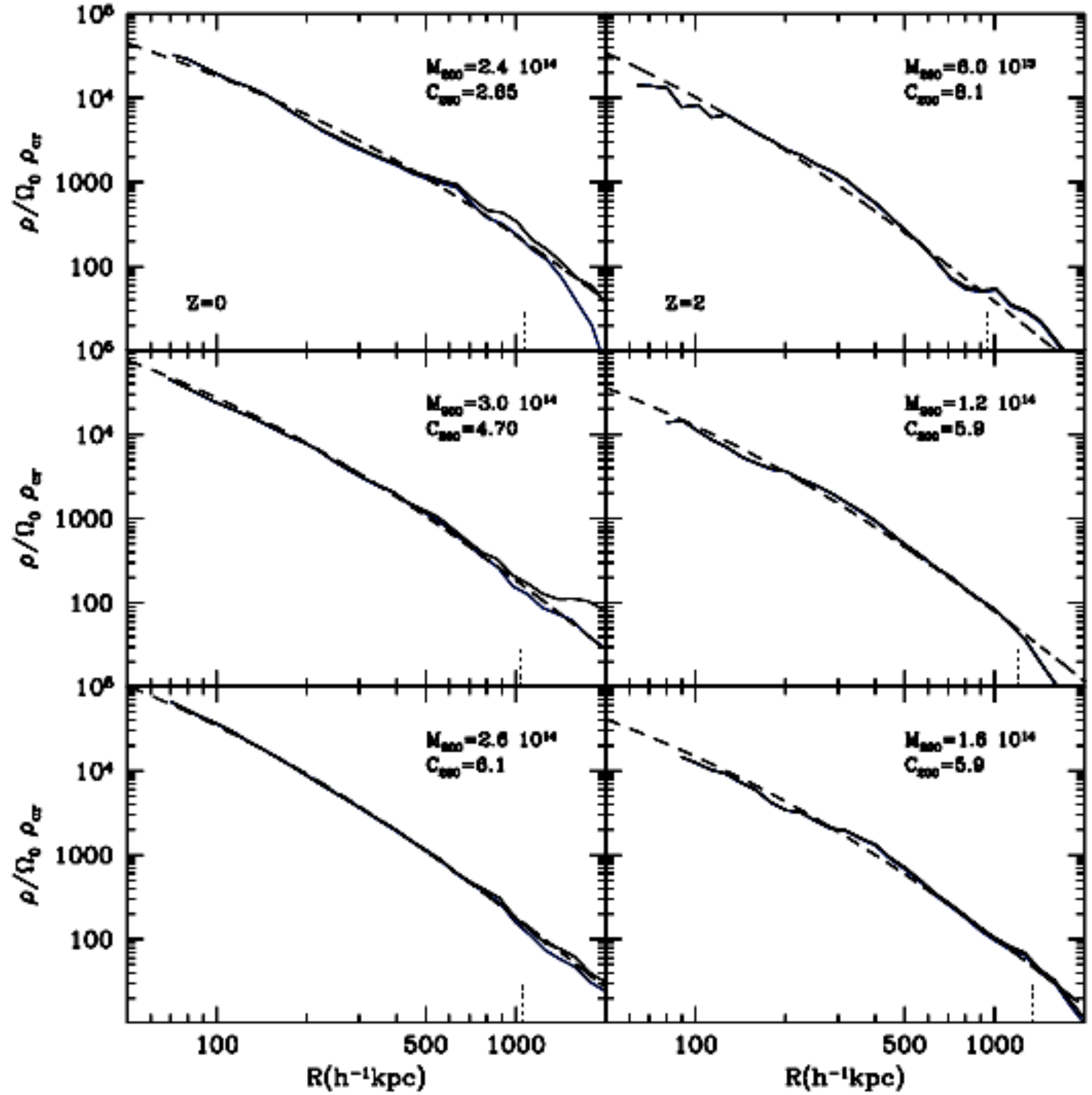

Figure 3. Examples of density profiles for cluster-size haloes (full curves) and their fits (dashed curves) using concentrations obtained with the ratios of the maximum circular velocity $V_{\rm max}$ to the halo velocity V_{200}. Panels on the left are for redshift $z = 0$ and the right-hand panels are for $z = 2$. Each panel shows two full curves: the density profile of all particles (upper curve) and only bound particles (lower curve). Vertical dotted lines show the outer radius of bound particles.

• Halo Concentrations

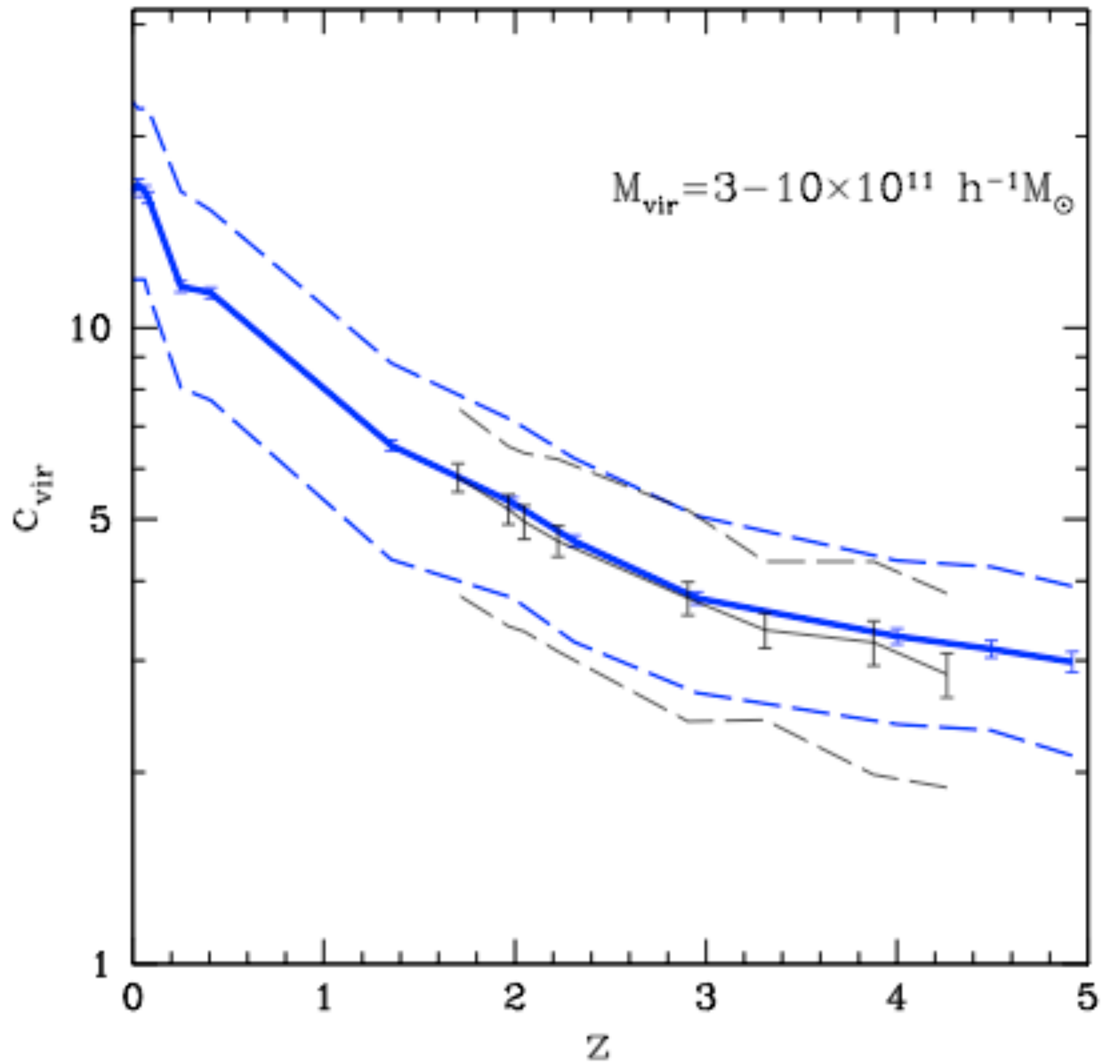

Figure 3. Convergence test for $c_{\rm vir}$ evolution and scatter. Shown is a comparison of $M_{\rm vir} = 3-10\times10^{11}h^{-1}M_\odot$ haloes simulated using our main simulation (thick lines) and a second simulation with 8 times the mass resolution (thin lines). The solid lines and errors reflect the median and Poisson uncertainty respectively. The dashed lines reflect the estimated intrinsic scatter. There is no evidence for significant deviations in either the measured median or scatter as the mass resolution is increased.

• Main trend with redshift

for a fixed halo mass

$$c_{\rm vir}(a) \propto a.$$

$$C \equiv \frac{r_{\rm vir}}{r_s}\,,$$

$$r_{\rm vir}(M_{\rm vir}) = 443\ h^{-1}\ {\rm kpc}\left(\frac{M_{\rm vir}/10^{11}\ h^{-1}\ M_\odot}{\Omega_0\,\delta_{\rm th}}\right)^{1/3}$$

$$M_{\rm vir} \equiv \frac{4\pi}{3}\,\rho_{\rm cr}\,\Omega_0\,\delta_{\rm th}\,r_{\rm vir}^3\ .$$

- Main trend with mass:

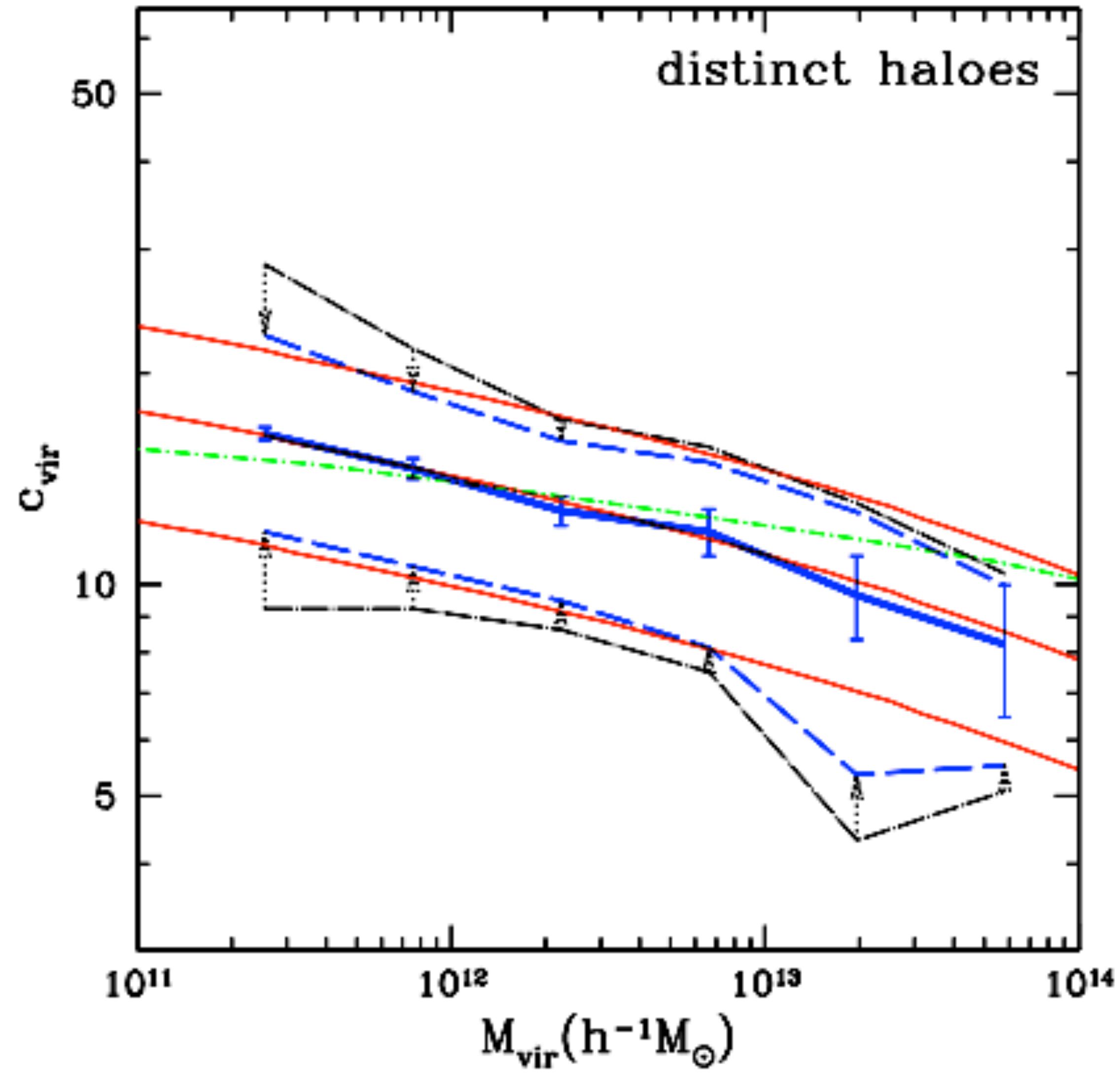

Figure 4. Concentration versus mass for distinct haloes at $z = 0$. The thick solid curve is the median at a given $M_{\rm vir}$. The error bars represent Poisson errors of the mean due to the sampling of a finite number of haloes per mass bin. The outer dot-dashed curves encompass 68% of the $c_{\rm vir}$ values as measured in the simulations. The inner dashed curves represent only the true, intrinsic scatter in $c_{\rm vir}$, after eliminating both the Poisson scatter and the scatter due to errors in the individual profile fits due, for example, to the finite number of particles per halo. The central and outer thin

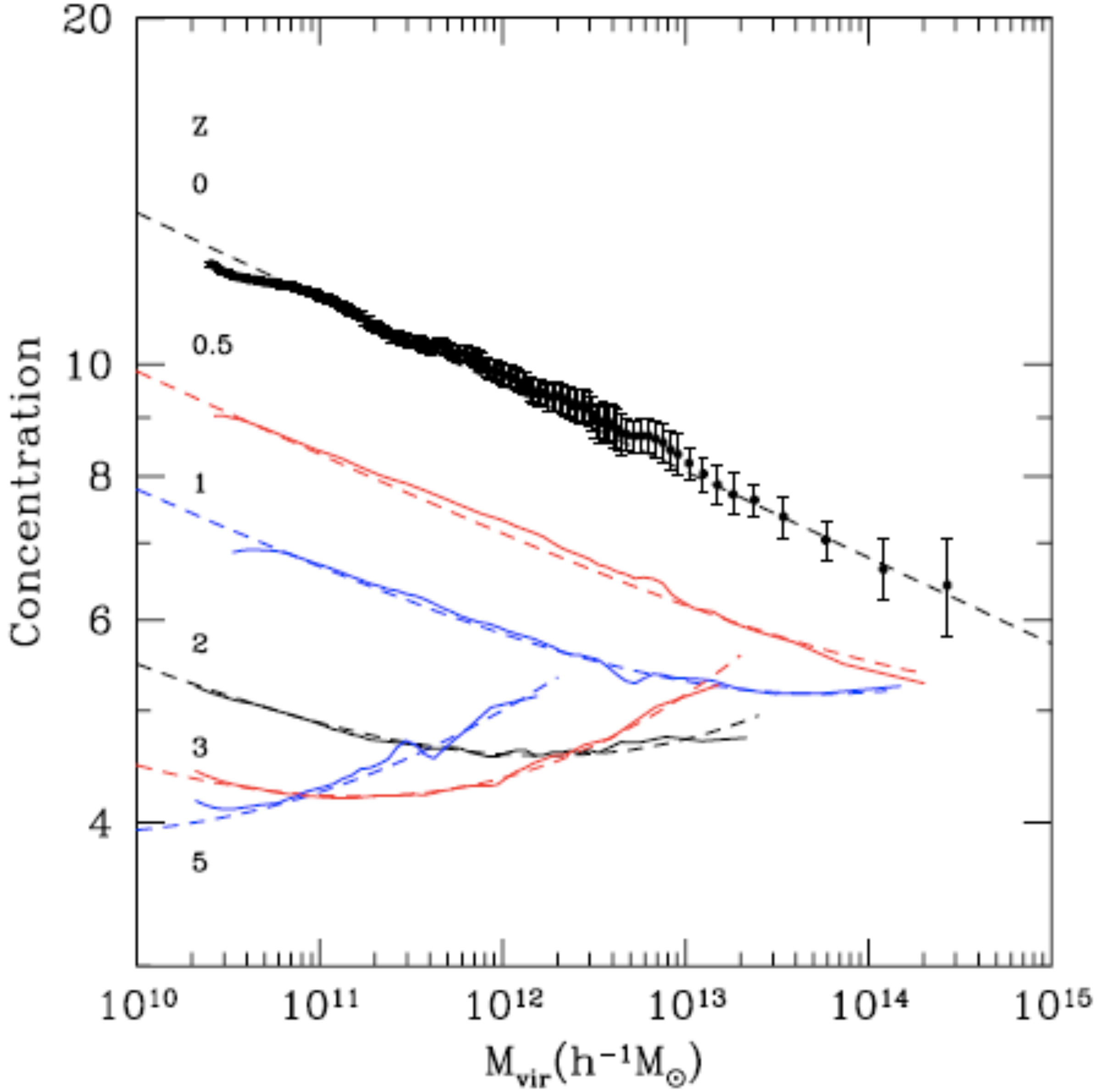

z=0 $$c(M_{\rm vir}) = 9.60 \left(\frac{M_{\rm vir}}{10^{12}\, h^{-1}\, M_\odot} \right)^{-0.075}$$

Figure 5. Evolution of concentration of distinct halos with redshift. The full curves and symbols show results of simulations. Analytical approximations are shown as dashed curves. All the fits have the same functional form of Equation (12) with two free parameters. At low redshifts the halo concentration decreases with increasing mass. However, the trend changes at high redshifts when the concentration is nearly flat and even has a tendency to slightly increase with mass.

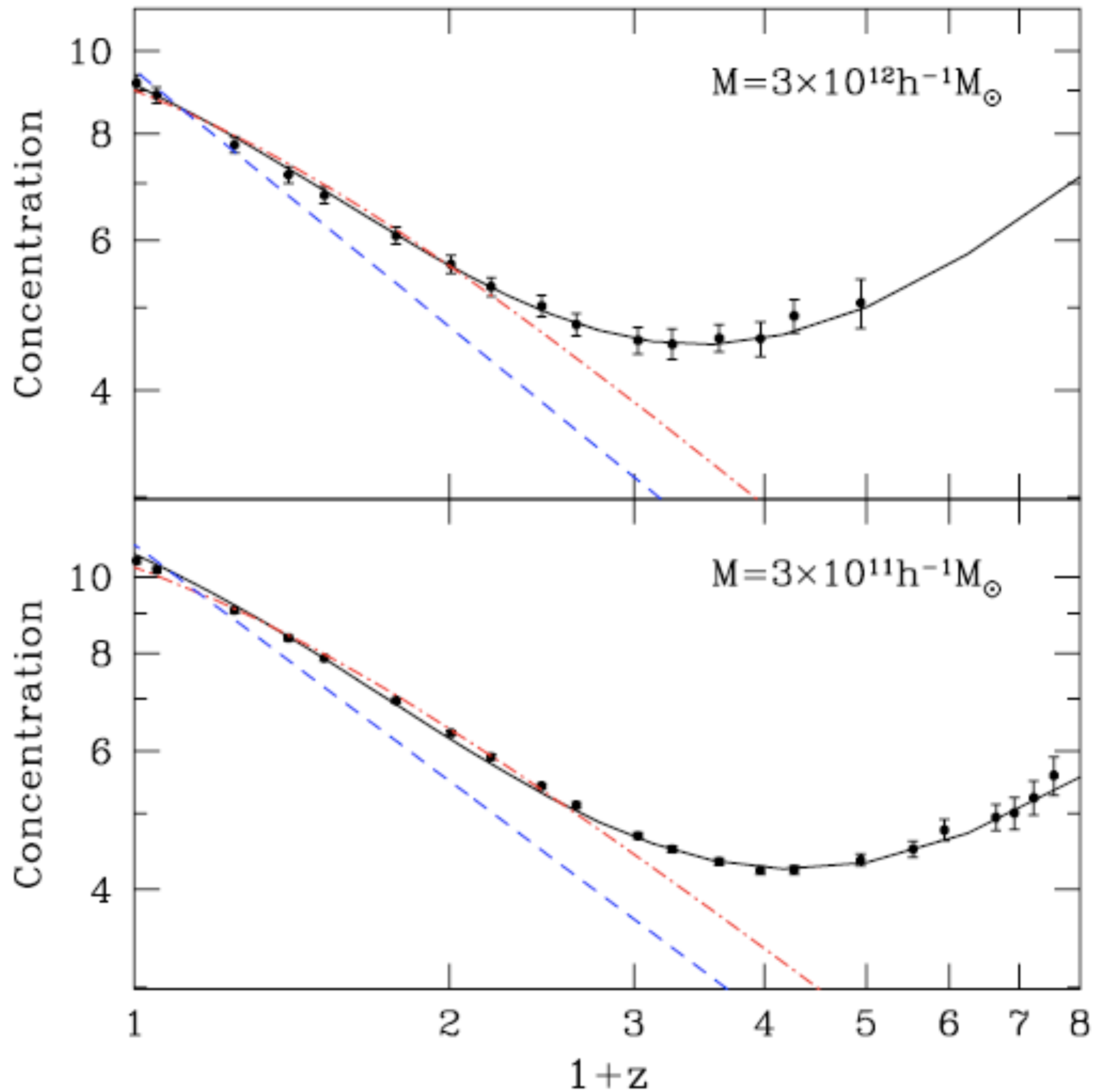

Figure 6. Evolution of halo concentration for halos with two masses indicated on the plot. The dots show results of simulations. For the reference the dashed lines show a power-law decline $c \propto (1+z)^{-1}$. Concentrations do not change as fast as the law predicts. At low redshifts $z < 2$ the decline in concentration is $c \propto \delta$ (dot-dashed curves), where δ is the linear growth factor. At high redshifts the concentration flattens and then slightly increases with mass. For both masses the concentration reaches a minimum of $c_{\rm min} \approx$ 4–4.5, but the minimum happens at different redshifts for different masses. The full curves are analytical fits with the functional form of Equation (13).

Halo Concentration: need to know to get density profile

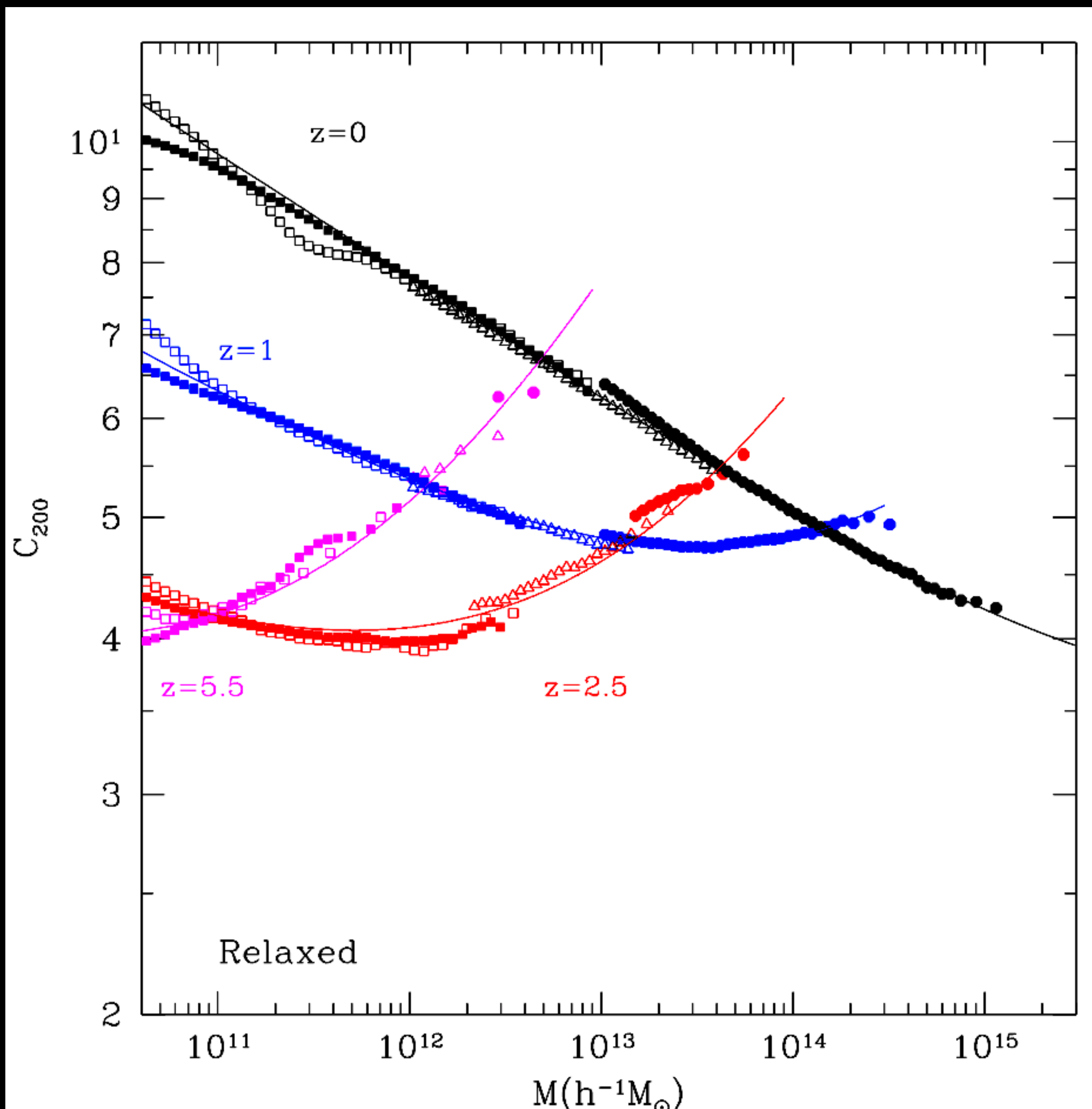

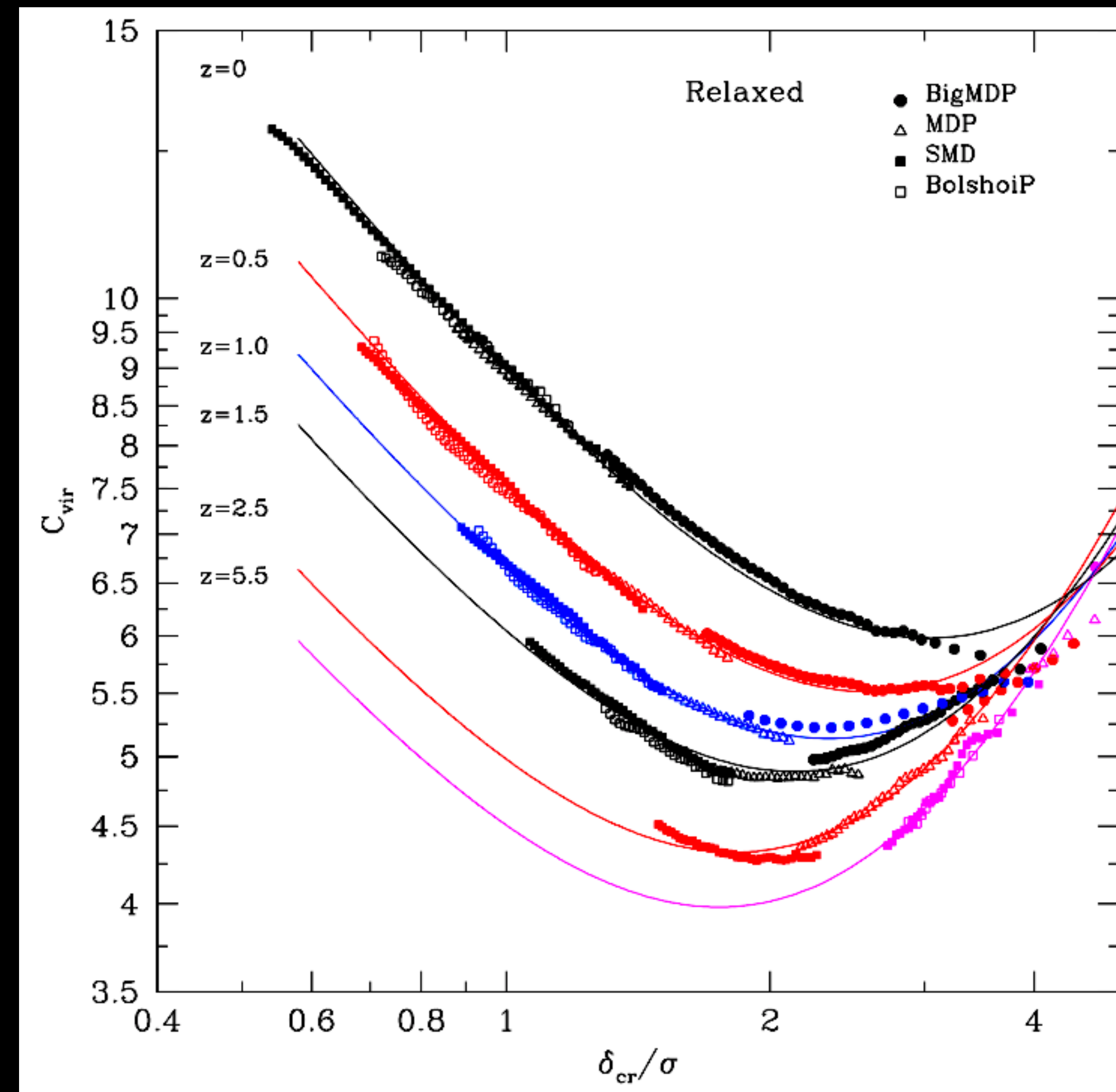

Klypin et al 2014: Gadget + ART

MultiDark suite of sims: 60G particles

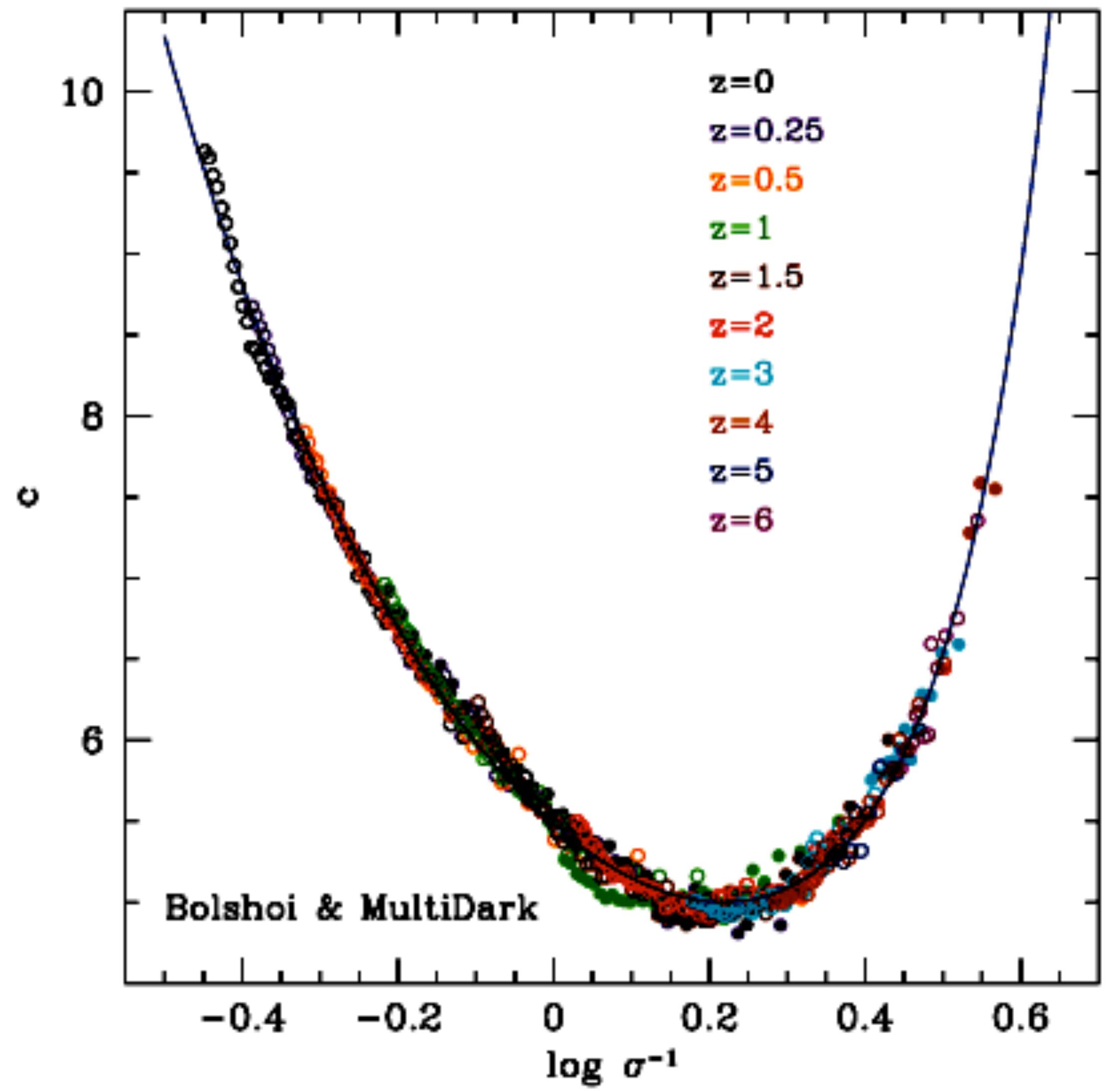

Figure 11. Dependence of halo concentration c on log σ^{-1} after rescaling all the results of Bolshoi and MultiDark simulations to $z = 0$. The plot shows a tight intrinsic correlation of $\mathcal{C}$ on σ'.

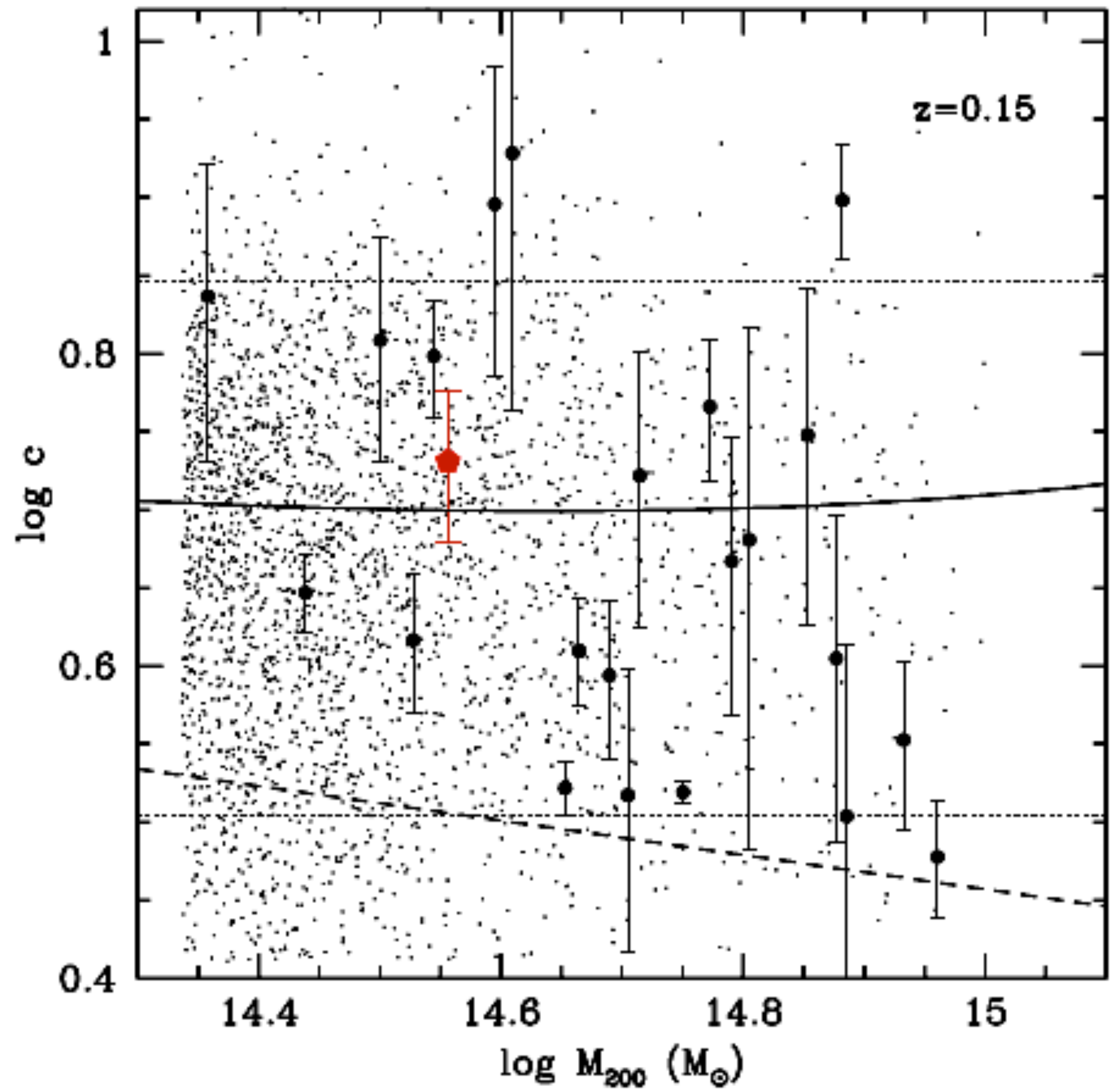

Figure 13. Comparison of observed cluster concentrations (open symbols with error bars) with the prediction of our model for median halo concentration of cluster-size haloes (full curve). Dotted lines show the 10 per cent and 90 per cent percentiles. We also show the concentrations, in the same mass interval, for all the individual simulated clusters found in the MultiDark simulation box (data points). Open circles show results for X-ray luminous galaxy clusters observed with *XMM–Newton* in the redshift range 0.1–0.3 (Ettori et al. 2010). The pentagon presents galaxy kinematic estimate for relaxed clusters by Wojtak & Łokas (2010). The dashed curve shows prediction by Macciò et al. (2008), which significantly underestimates the concentrations of clusters.

Effects of selection: relaxed halos are more concentrated

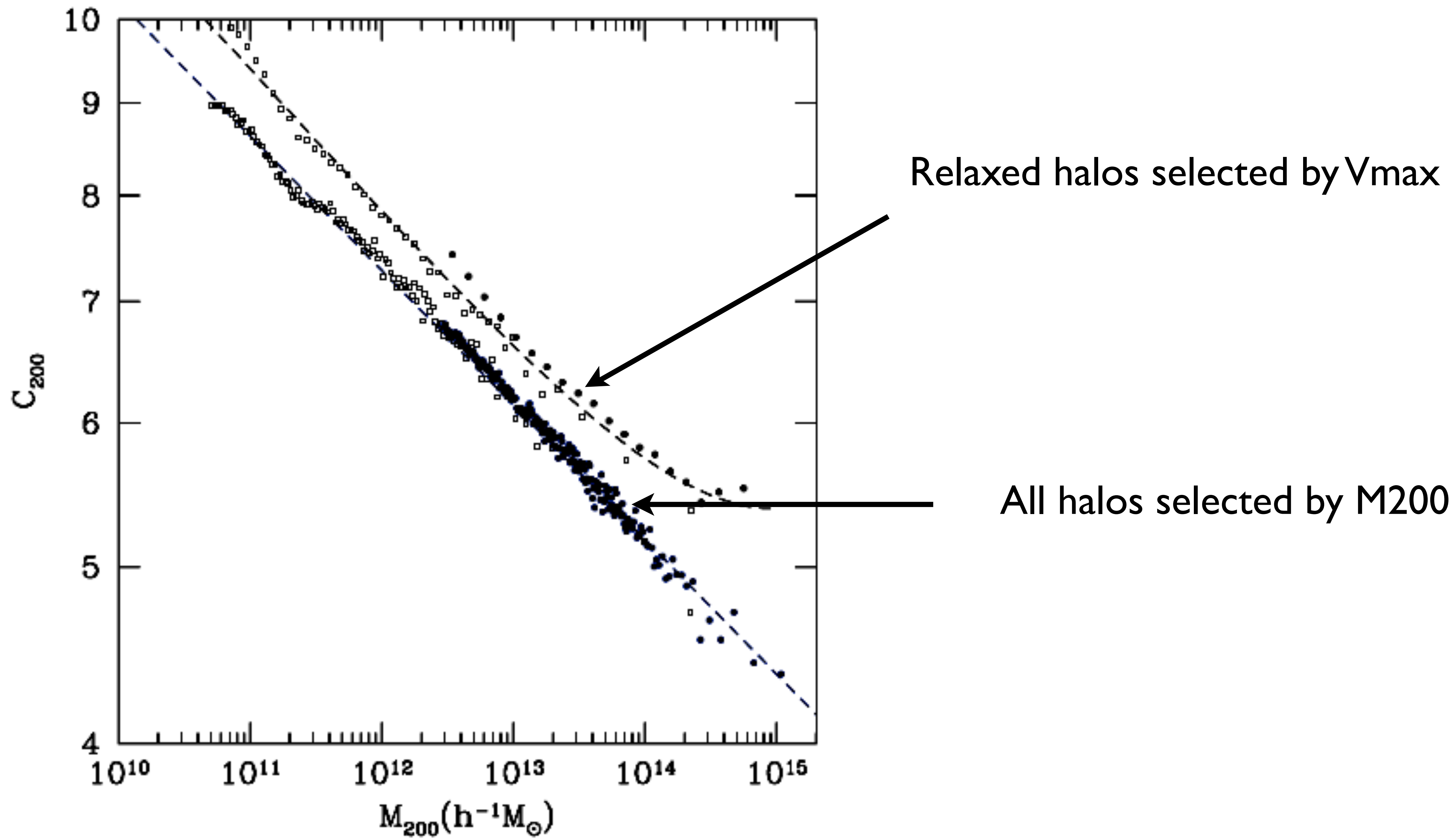

z=0

Densities and velocities at large distances

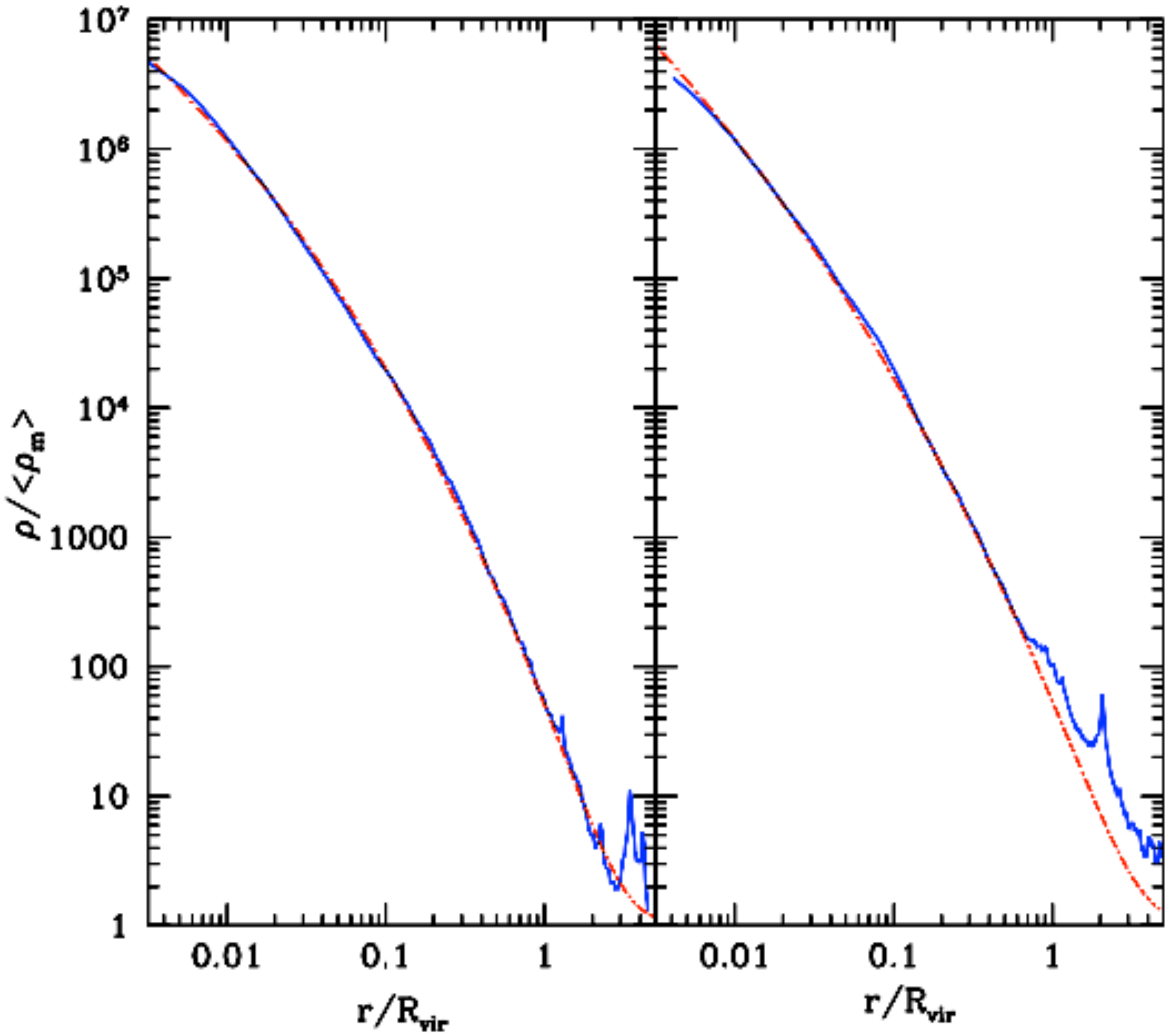

Fig. 1.— Dark matter density profiles of two dark matter halos (full curves) in the simulation Box20. The halos have virial masses of $1.4 \times 10^{12} h^{-1} M_\odot$ (left panel) and $2.6 \times 10^{11} h^{-1} M_\odot$ (right panel). The larger halo has a neighbour at 3.5 R_{vir} which is the halo on the right panel. This smaller halo is responsible for the spike at large radii in the density profile. In turn, the halo on the right panel has its own smaller neigbour at $2R_{vir}$ observed as a spike and an extended bump in the density profile. The dashed curves show the 3D Sersic profiles. The halo density profiles extend well beyond the formal virial radius with the Sérsic profile providing remarkably good fits.

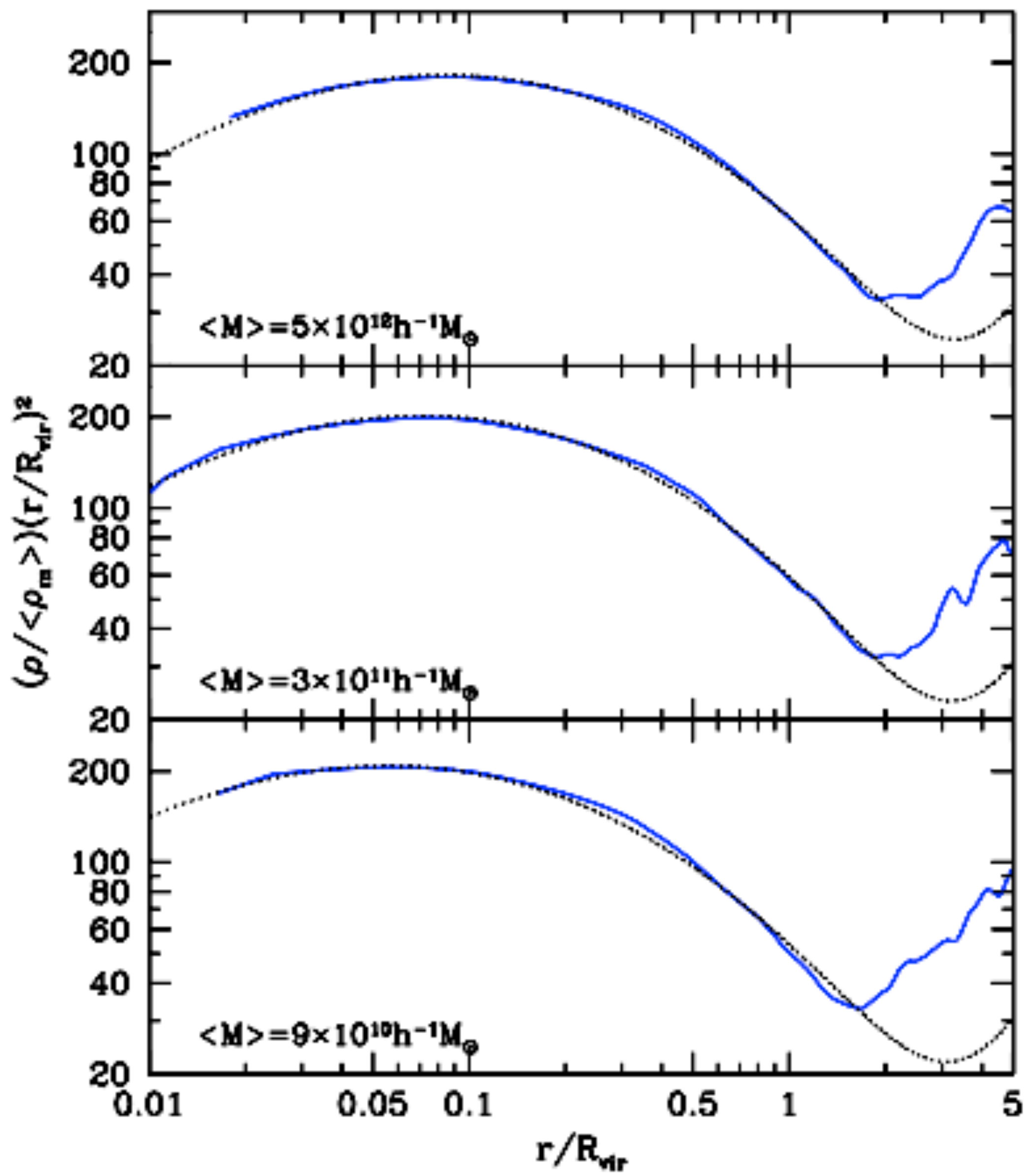

Fig. 3.— Average density profiles for halos with different virial masses. The 3D Sérsic profile provides very good fit with few percent errors within $2R_{\rm vir}$. Even at $3R_{\rm vir}$ the error is less than 20-30 percent. The density profiles are well above the average density of the Universe throughout all the radii.

Phase-space diagram for the particles in dark matter halos

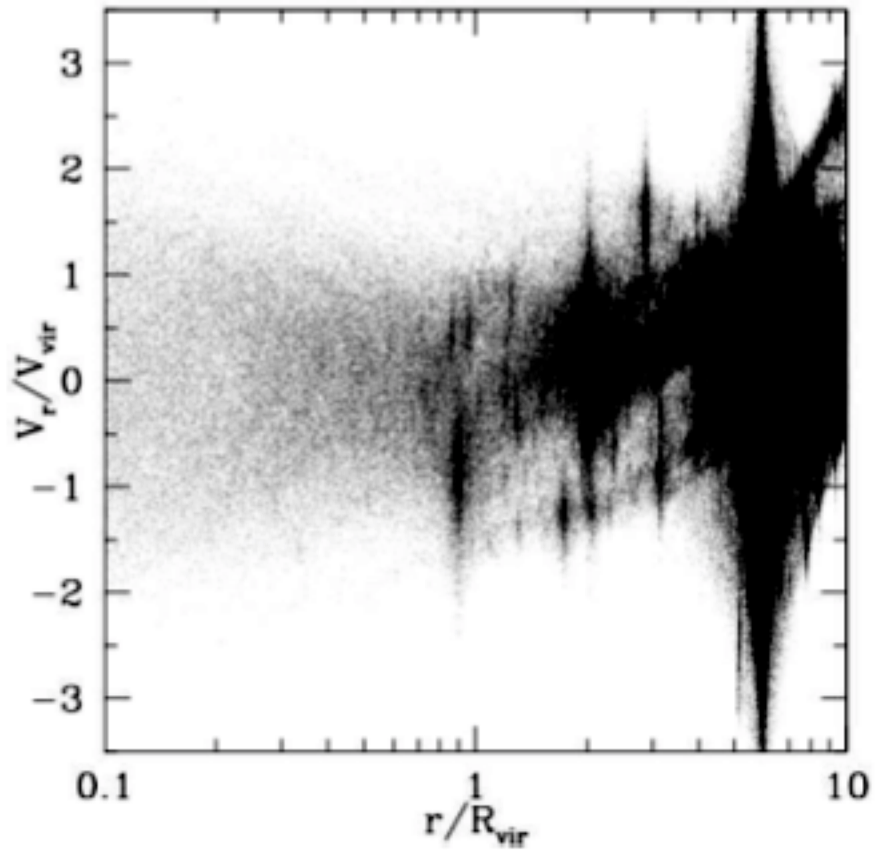

Mvir =3 10^{11}Msun

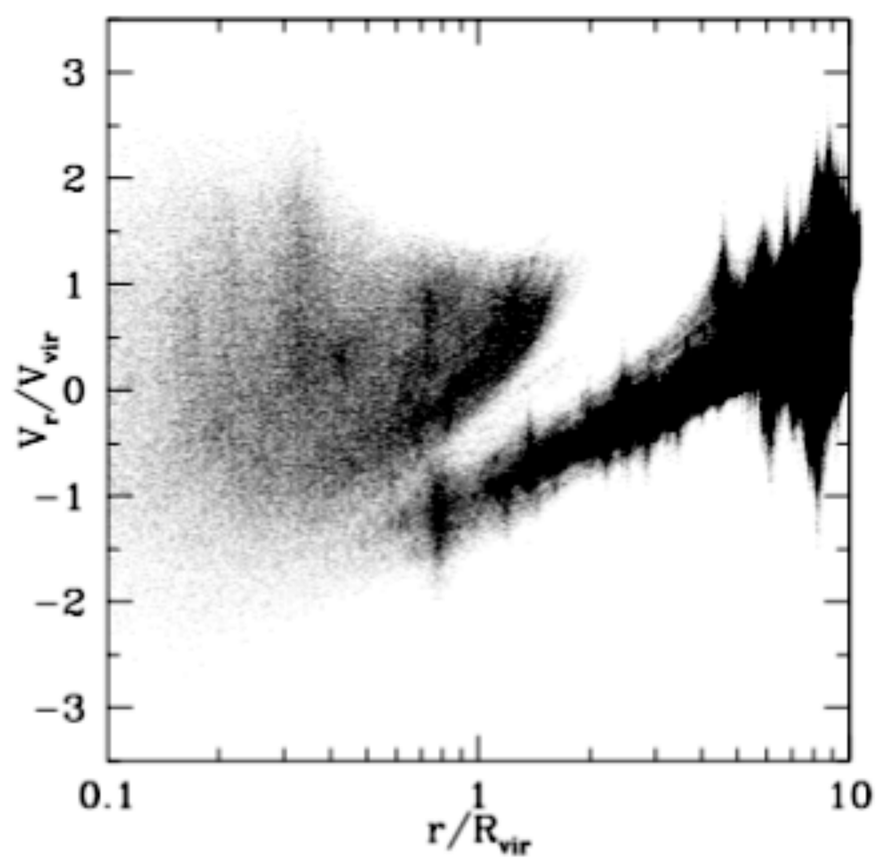

Mvir =1.5 10^{15}Msun

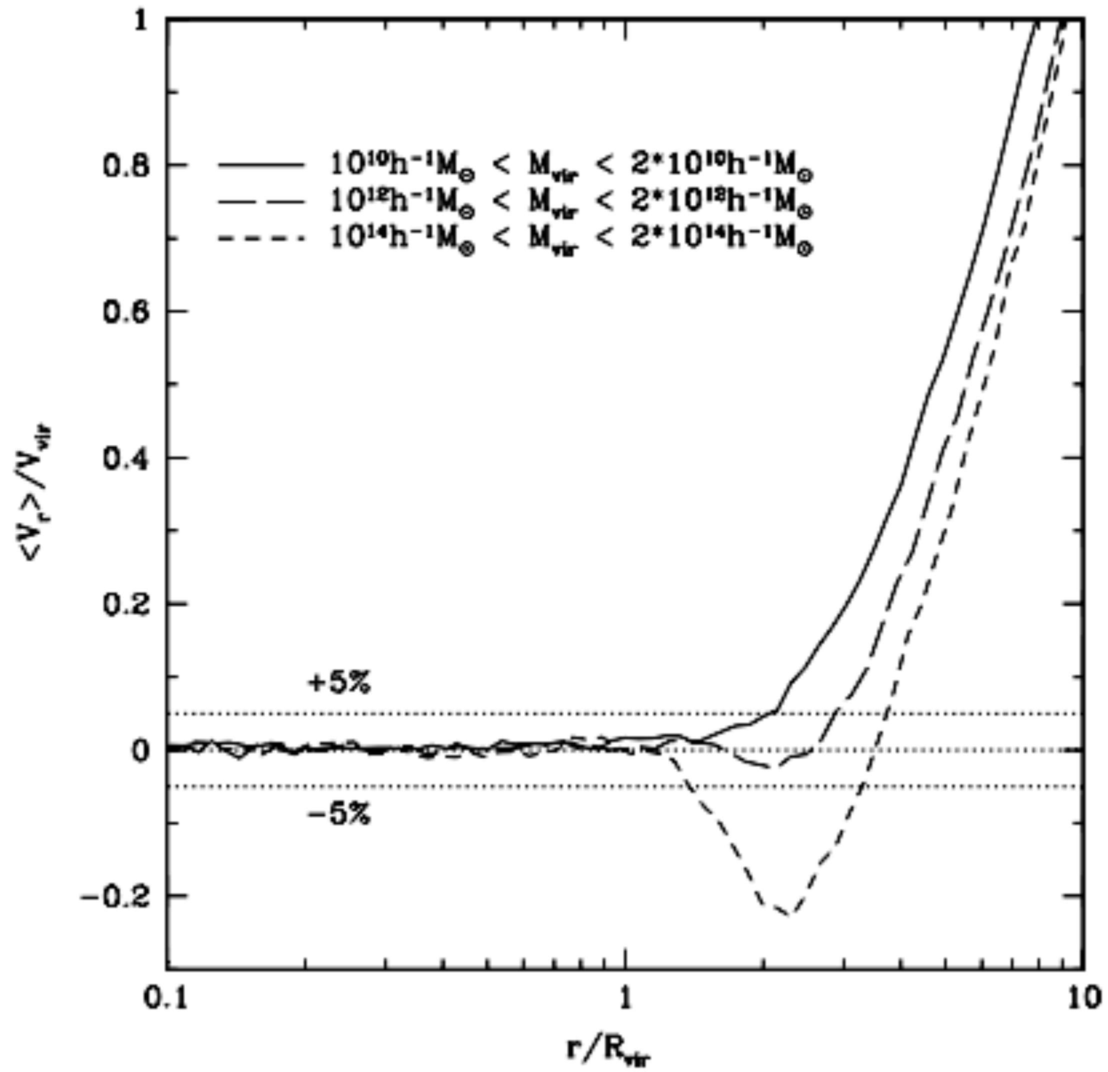

Figure 4. Mean radial velocity for three different mass bins. The profiles were obtained by averaging over hundreds of distinct haloes on each mass bin. In dotted line is shown the selected threshold delimiting the static region (5 per cent of the virial velocity). Cluster-size haloes display a region with strong infall (dashed line). On the contrary, low-mass haloes (solid line) and galactic haloes (long-dashed line) do not show infall at all but a small outflow preceding the Hubble flow.

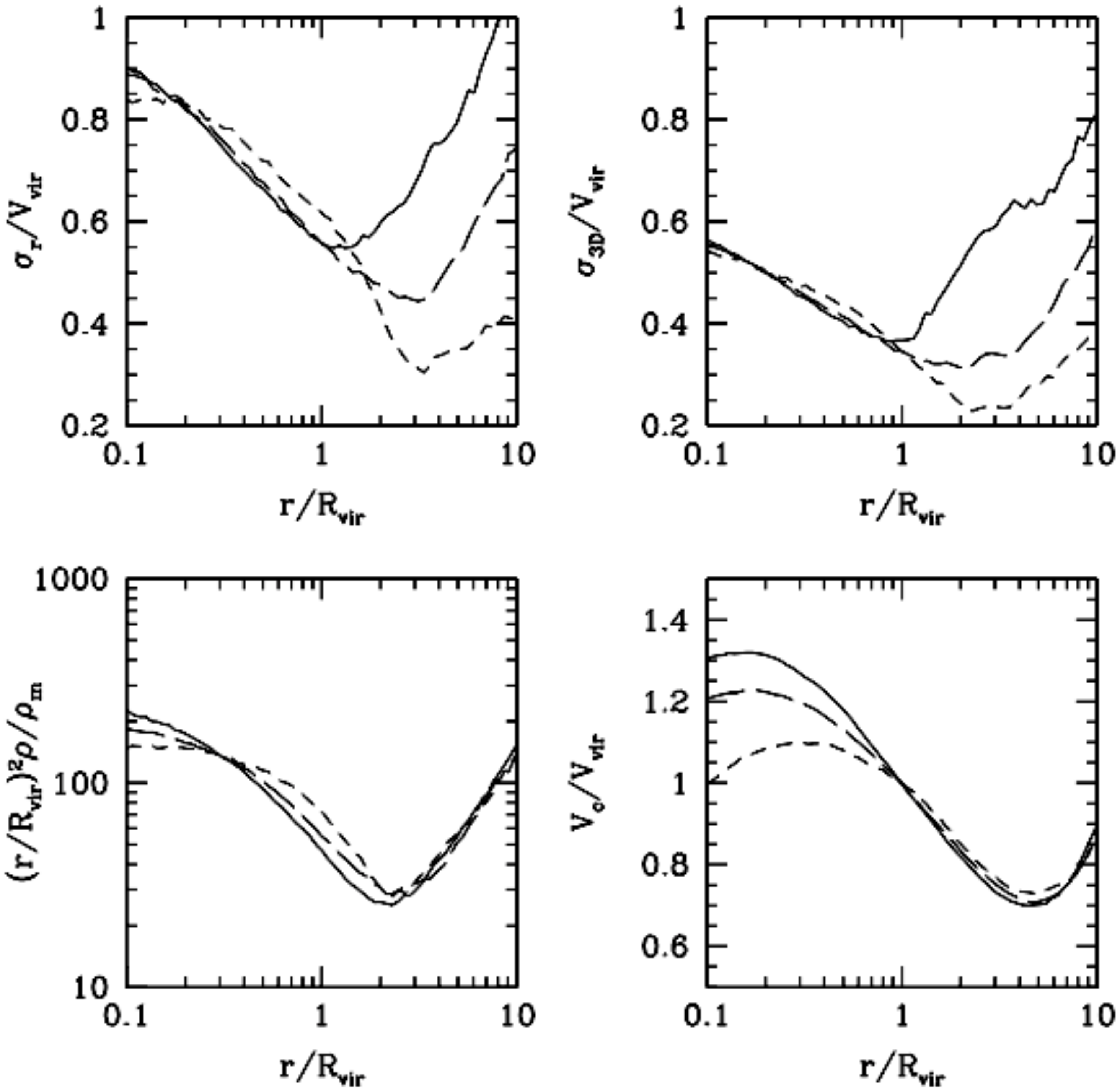

Figure 5. Median profiles for the same halo mass bins as in Figure 4. These profiles show how the behaviour of haloes depends on the halo mass. Top left panel: radial velocity dispersion. Top right: 3D velocity dispersion. Bottom left: density profile. Bottom right: Circular velocity profile. The different line styles represent the same mass bins as in Figure 4.

Infall velocities on halos.

nu = peak height = δ_{cr}/σ

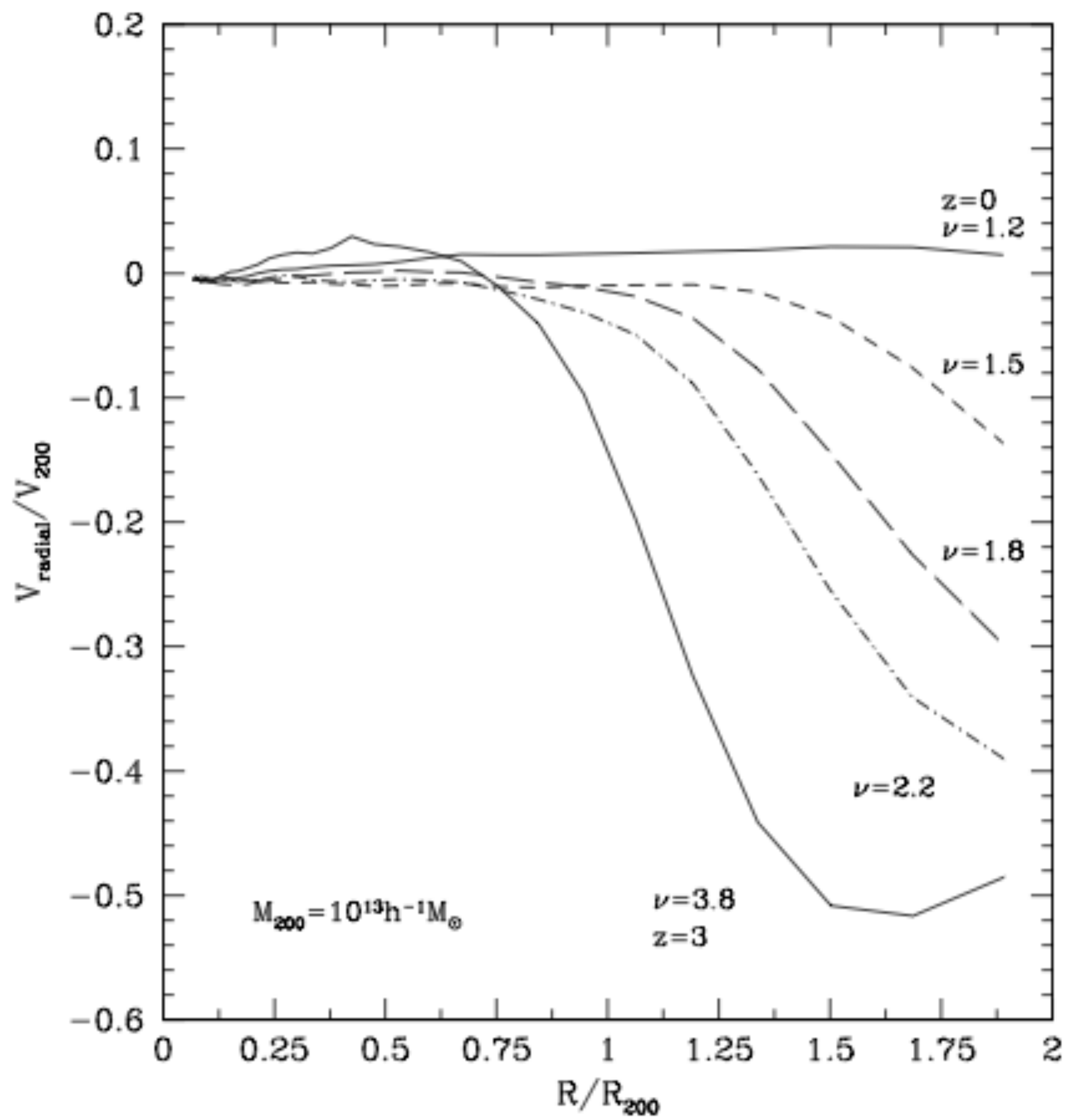

Velocity anisotropy

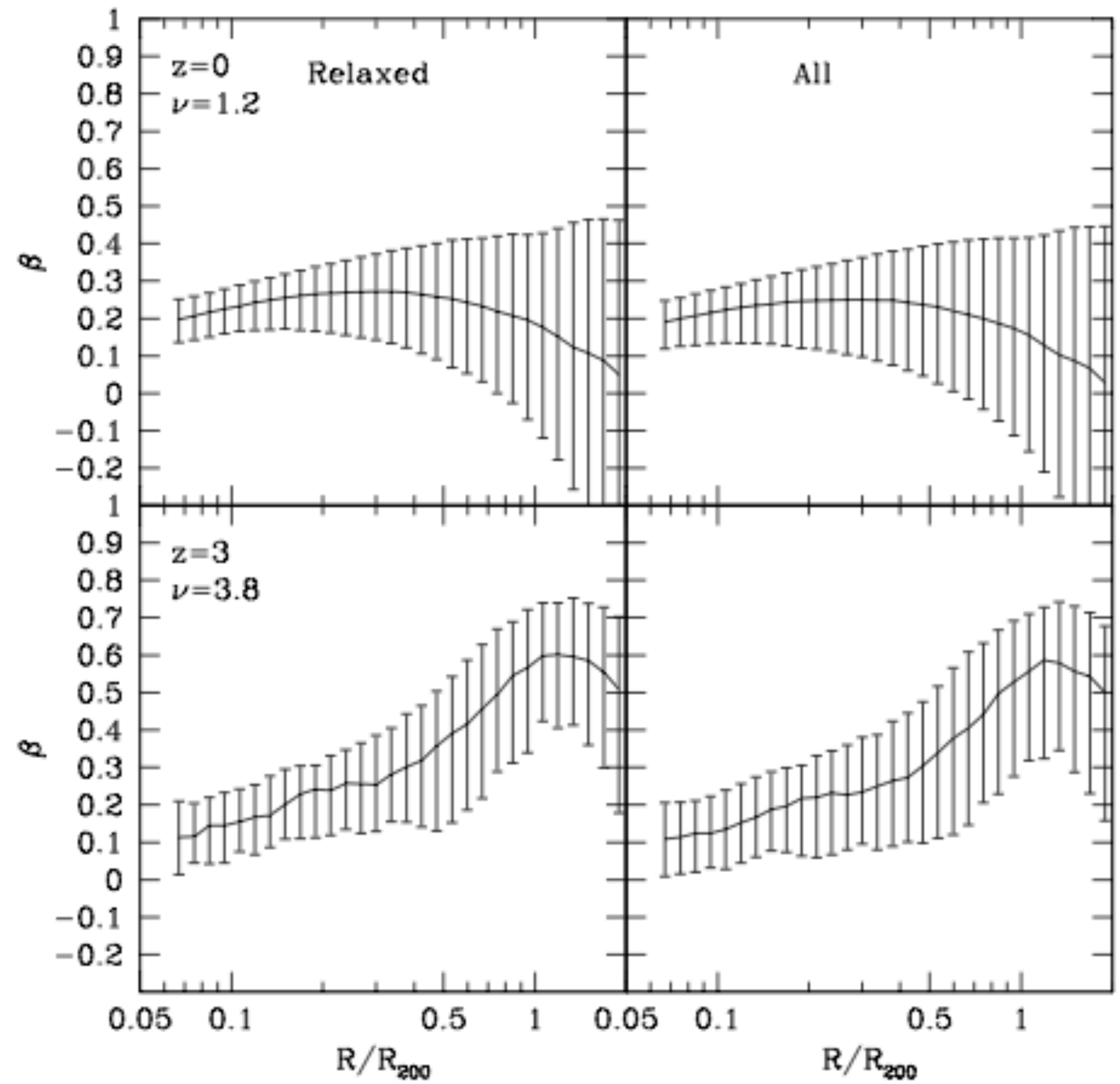

δ_{cr}/σ

Mass at ~1 kpc radius. Overabundance problem

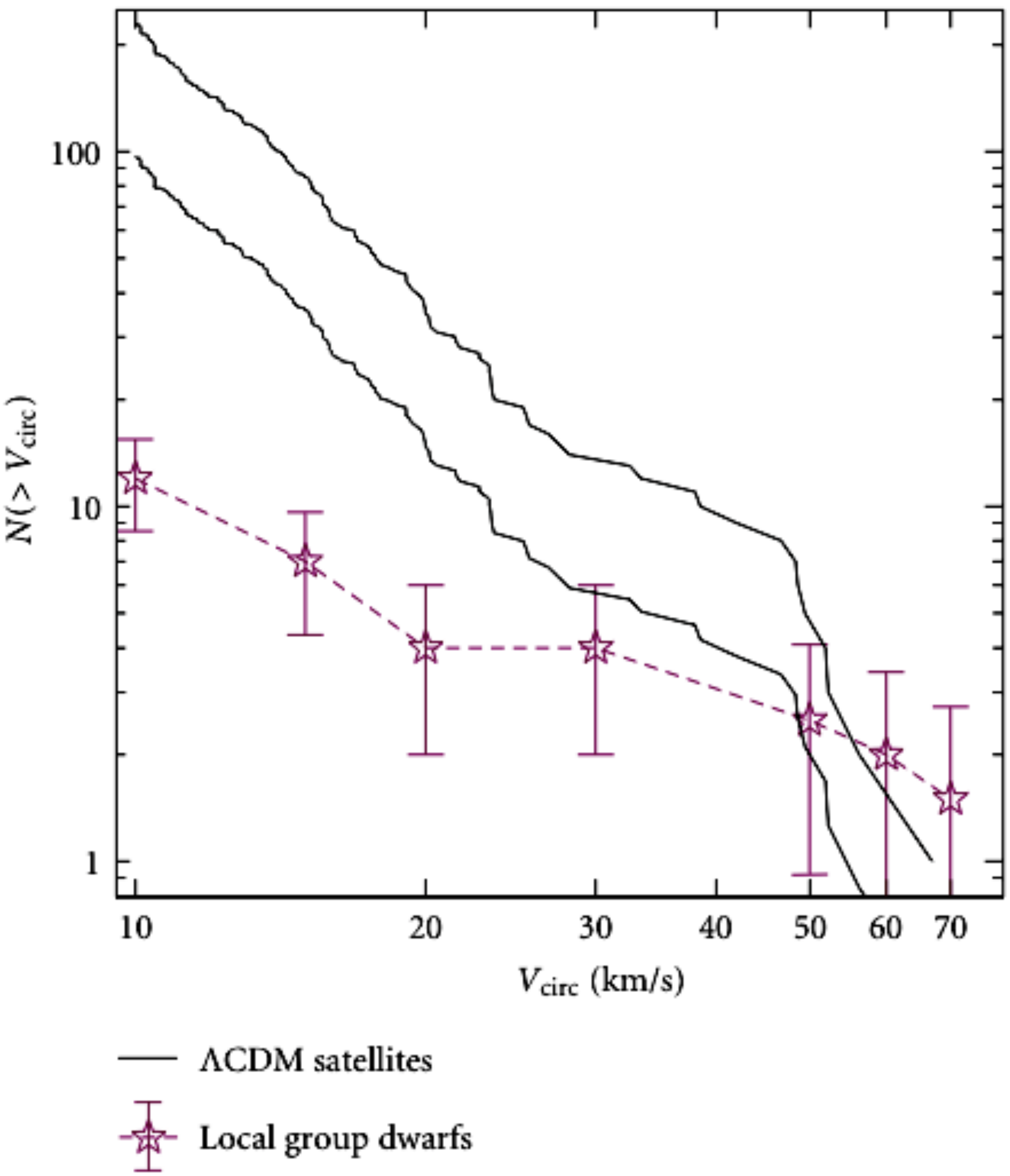

FIGURE 7: Comparison of the cumulative circular velocity functions, $N(> V_{max})$, of subhalos and dwarf satellites of the Milky Way within the radius of 286 kpc (this radius is chosen to match the maximum distance to observed satellites in the sample and is smaller than the virial radius of the simulated halo, $R_{337} = 326$ kpc). The subhalo VFs are plotted for the host halos with maximum circular velocities of 160 km/s and 208 km/s that should bracket the V_{max} of the actual Milky Way halo. The VF for the observed satellites was constructed using circular velocities estimated from the line-of-sight velocity dispersions as $V_{max} = \sqrt{3}\sigma_r$ (see the discussion in the text for the uncertainties of this conversion).

Kravtsov 2009

Subhalos

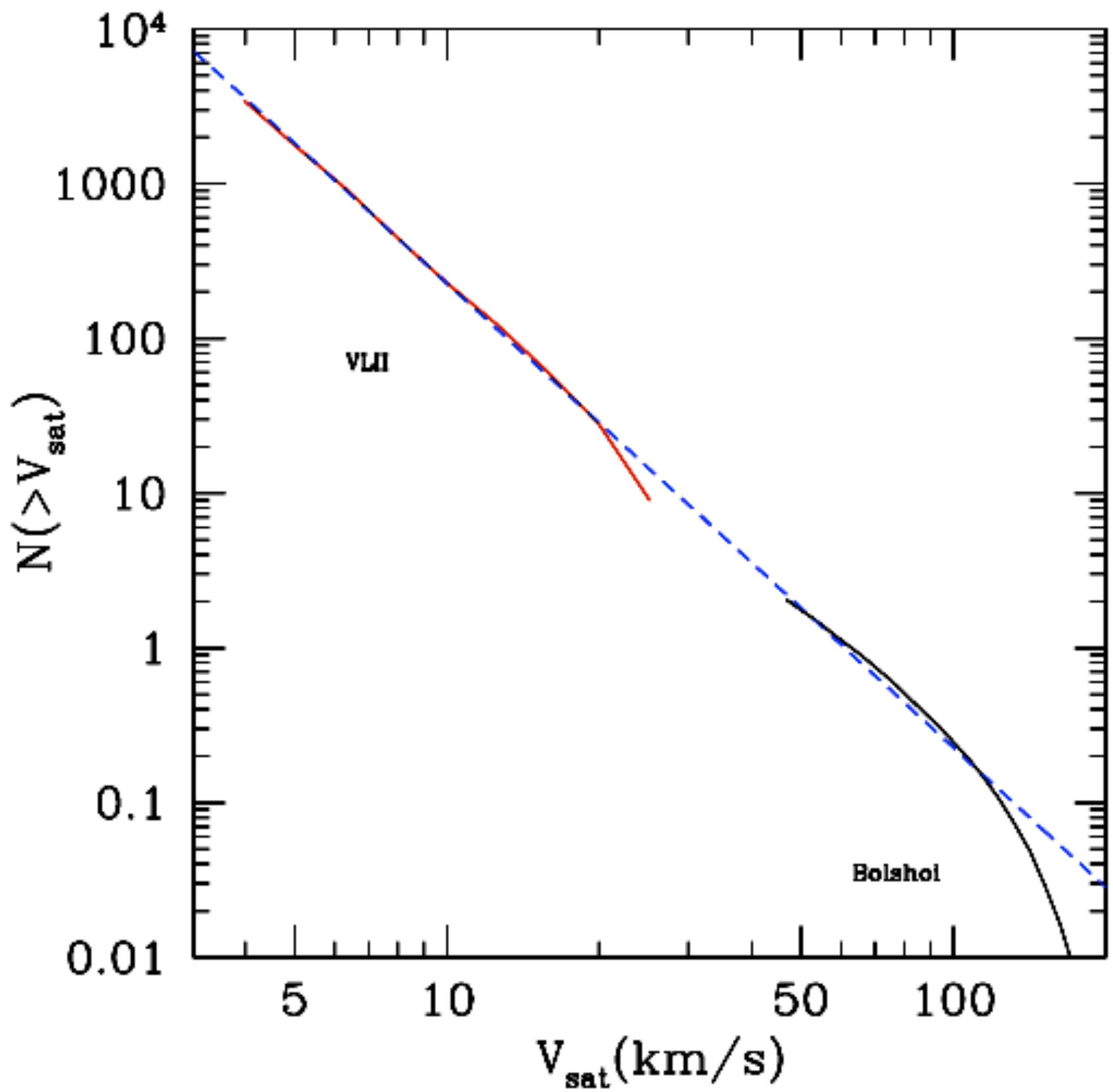

Figure 14. Comparison of satellite velocity functions in the Via Lactea-II and Bolshoi simulations for host halos with $V_{\rm circ} = 200$ km s^{-1} and $M_{\rm vir} \approx 1.3 \times 10^{12}\, h^{-1}\, M_\odot$. The dashed line is a power law with slope -3, which provides an excellent fit to both simulations. In both simulations satellites are found inside a sphere with virial radius $R_{\rm vir}$.

$$N(>x) = 1.7 \times 10^{-3} V_{\rm host}^{1/2} x^{-3},$$

$$x \equiv V_{\rm sub}/V_{\rm host}, \quad x < 0.7,$$

Number-density profile of satellites

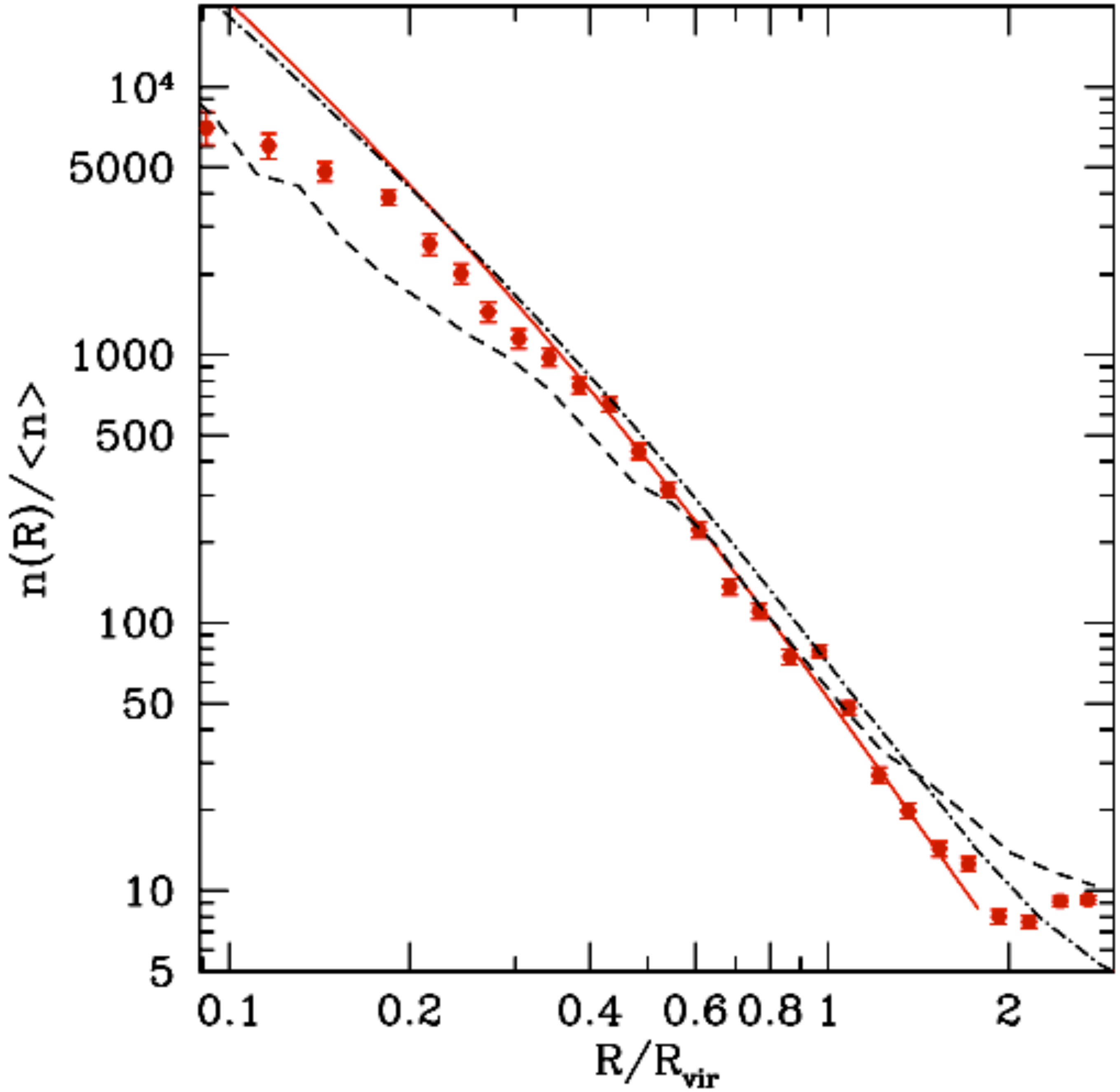

Figure 15. Density profiles for galaxy-size halos with $V_{\rm circ} \approx 200$ km s^{-1}. The full curve and circles are the dark matter density and the number density of satellites with $V_{\rm circ} > 4$ km s^{-1} in the Via Lactea-II simulation normalized to the average (number-)density for each component, respectively. The satellites have nearly the same overdensity as the dark matter for radii $R = (0.3\text{–}2)R_{\rm vir}$. The number density of satellites falls below the dark matter at smaller radii. The dashed curve is the number density of satellites with $V_{\rm circ} > 80$ km s^{-1} found at $z = 0$ in the Bolshoi simulation for host halos selected to have the same circular velocity as Via Lactea-II. In the outer regions with $R = (0.5\text{–}1.5)R_{\rm vir}$ the satellites follow the dark matter very closely. In the inner regions the Bolshoi results are 20%–30% below the much higher resolution simulation Via Lactea-II, presumably because of numerical effects.